This is the peer-reviewed, final accepted version for American Mineralogist, published by the Mineralogical Society of America.
The published version is subject to change. Cite as Authors (Year) Title. American Mineralogist, in press.
DOI: https://doi.org/10.2138/am-2022-8395. http://www.minsocam.org/

# REVISION 1

# Lifting the cloak of invisibility: gold in pyrite from the Olympic Dam Cu-U-Au-Ag deposit, South Australia

Kathy Ehrig[1,2,*], Cristiana L. Ciobanu[3], Max R. Verdugo-Ihl[3], Marija Dmitrijeva[3], Nigel J. Cook[2], Ashley Slattery[4]

[1]*BHP Olympic Dam, 10 Franklin Street, Adelaide, SA 5000, Australia*

[2]*School of Civil, Environmental and Mining Engineering, The University of Adelaide, Adelaide, SA, 5005, Australia*

[3]*School of Chemical Engineering and Advanced Materials, The University of Adelaide, Adelaide, SA, 5005, Australia*

[4]*Adelaide Microscopy, The University of Adelaide, Adelaide, SA, 5005, Australia*

## Abstract

'Invisible gold' refers to gold (Au) occurring either within the lattice of a host sulfide or as discrete nanoparticles (NPs, <100 nm-diameter) within a host that are only observable when imaged at higher magnifications. Previous research has regarded the physical form of invisible gold to be partially controlled by the concentration of arsenic (As) in the host sulfide, with stability fields for lattice-bound versus Au-NPs defined by an empirical Au-As solubility curve. We undertook micron- and nanoscale analysis of a representative sample of As-Co-Ni-(Au)-bearing pyrite from Cu-mineralized breccias in the deeper part of the Olympic Dam Cu-U-Au-Ag deposit (South Australia) to define the location and physical form of Au and accompanying elements. Trace element geochemistry and statistical analysis show that >50% of pyrites contain measurable Au and As, and plot below the Au-As solubility curve. Gold and As are geochemically associated with Te, Bi, Pb, Ag and Sn. Primary oscillatory zoning patterns in pyrite defined by As-Co-Ni are reshaped by processes of dissolution-

* Corresponding author. kathy.ehrig@bhp.com

reprecipitation, including new nanoscale growth and rhythmical misorientation structures. Low-angle slip dislocations, twist-wall boundaries and deformation-dipole nanostructures are associated with Te-Bi-Pb-enrichment and host Au-Ag-telluride nanoparticles (NPs). Electrum NPs occur associated with pores coated by Bi-Ag-tellurides or within chalcopyrite particles. Bi-Pb-sulfotellurides, petzite and sylvanite were identified by atomic-scale scanning transmission electron microscopy. The data support trace element (re)mobilization during pyrite deformation at the brittle to ductile transition (0.5-1 kbar, 300-400 °C) during brecciation. Au-NP formation is decoupled from initial As incorporation in pyrite and instead fingerprints formation of strain-induced, chalcogen-enriched nanoscale structures. Pore-attached NPs suggest scavenging of Au by Bi-bearing melts with higher rates of fluid percolation. Similar scenarios are predictable for pyrite-hosted 'invisible Au' in pyrite from other deposits that experienced multiple overprints. Unveiling the cloak of invisibility using contemporary micro- to nano-analytical techniques reveals new layers of complexity with respect to the trace/minor element incorporation in mineral matrices and their subsequent release during overprinting.

**Keywords**: Pyrite; Invisible gold; Au-Ag-tellurides; Bi-Pb-(sulfo)tellurides; Olympic Dam; HAADF STEM

## Introduction

"Invisible gold" (Cook and Chryssoulis, 1990) refers to gold that is either present within solid solution (hosted directly in the crystal lattice), or as discrete inclusions of gold, electrum or other Au-bearing minerals, <1 μm in size, within a host mineral, commonly pyrite or arsenopyrite. Such gold is undetectable by conventional optical or scanning electron microscopy (SEM). Since the first visualization of a gold nanoparticle in pyrite (Palenik et al., 2004), rapid advances in *in-situ* microanalytical techniques and case studies of invisible gold in different ore types have enabled the physical and chemical state of Au in pyrite to be characterized in ever greater detail and at ever better spatial resolutions. This empirical data has been accompanied by various experimental studies as well

as thermodynamic modelling that has advanced understanding of the mechanisms involved and the geochemical controls on incorporation of invisible gold within common sulfides (e.g., Reich et al., 2005; Deditius et al., 2008; Cook et al., 2013; Fougerouse et al., 2016a, 2016b; 2021; Pokrovski et al., 2019, 2021; Xing et al., 2019).

Incorporation of Au into pyrite is considered to be mediated by arsenic (Reich et al., 2005; Deditius et al., 2014), with many examples of Au-bearing arsenian pyrite documented from a wide range of deposit types (e.g., Morey et al., 2008; Large et al., 2009; Gregory et al., 2015; Li et al., 2019; Morishita et al., 2019). Reich et al. (2005) proposed an empirical model for gold in pyrite and defined a maximum solubility limit of Au in pyrite that can be related to As content. The relationship was defined as $C_{Au} = 0.02 \times C_{As} + 4 \times 10^{-5}$, where C represents concentration (mol%).

Recently, geochemical modelling coupled with high-resolution X-ray absorption spectroscopy data allowing identification of Au-As-S-complexes, led Pokrovski et al. (2021) to postulate an overarching "arsenic-driven pump for invisible gold in hydrothermal systems". This model was considered to not only explain Au-enrichment in pyrite but also in arsenopyrite and löllingite.

Although arsenic is widely considered essential for Au incorporation in pyrite, examples of low-As pyrite containing significant concentrations of invisible gold are also known (e.g., Cook et al., 2009). Arsenic-Au decoupling has been interpreted to occur during rapid pyrite crystallisation (Wu et al., 2021) and a correlation between Au and Sb, instead of Au-As, was identified in distinct pyrite and arsenopyrite generations from a sulfosalt-rich, slate-hosted deposit (Li et al., 2019). Moreover, pore-attached Au-Ag-telluride nanoparticles, often also containing other elements (notably Pb but no Bi) have been observed along microfractures within As-free pyrite (Ciobanu et al., 2012), implying alternative mechanisms for trapping of invisible gold.

Trace element incorporation into, and release from a host mineral, are dependent upon the ability of the crystal structure to respond to strain induced by stress during geological events. Numerous studies, using either transmission electron microscopy (TEM) (e.g., van Goethem et al., 1978; Couderc et al., 1980; Graf et al., 1981; Cox et al., 1981, Levade et al., 1982; Cox, 1987), or electron

backscatter diffraction (EBSD; e.g., Boyle et al., 1998; Freitag et al., 2004; Barrie et al., 2008, 2009, 2010a, 2010b), have addressed the microstructures assisting deformation in pyrite at brittle-to-plastic transition conditions.

The deformation mechanism map for pyrite constructed by Barrie et al. (2011) indicates ductile behavior at temperatures as low as ~260 ºC, far lower than previously believed (Cox et al., 1981; McClay and Ellis, 1983), meaning that pyrite microstructures can be modified without deep burial metamorphism. The brittle to ductile transition is associated with a variety of deformation microstructures in pyrite, including low-angle (~2º) sub-grain boundaries or 'dislocation walls', indicating that both dislocation glide and creep operate during pyrite deformation (Barrie et al., 2009). The behavior of pyrite across the brittle-plastic transition is critical for understanding trace element behavior in pyrite because of how the crystal structure will accommodate defects and potentially promote incorporation of trace elements (Reddy and Hough, 2013), whether this takes place via crystal-plastic dislocation nucleation at crack-tips (Rogowitz et al., 2018), or glide planes associated with deformation dipoles and loops (Graf et al., 1981). Deformation-dipole models (DDM) are applicable to dislocations in crystals otherwise considered too brittle to undergo plastic deformation, as demonstrated for MgO ceramics (Amodeo et al., 2018). The splitting of long dipoles into loops associated within sulfur vacancies in pyrite were attributed to plastic deformation at 200-400 °C (Graf et al., 1981). Understanding of the microstructural evolution of pyrite crystals and the mechanisms that control accommodation of defects critical for doping, including clustered S vacancies remains incomplete. This is despite of surging interest from the materials science community as pyrite is recognized as a plentiful, albeit imperfect, low-cost photovoltaic material for production of thin-film solar cells (Gong et al., 2013; Voigt et al., 2019; Ray et al., 2020).

Despite the advances in understanding pyrite deformation and the incorporation and release of 'invisible gold' in pyrite over the past 40 years, the topic has remained largely unexplored in some deposit types characterized by complex mineralogy and geochemistry, notably iron-oxide copper gold deposits. Recent trace element data for pyrite from the >10 billion tonne Olympic Dam Cu-U-Au-Ag

deposit, South Australia (Dmitrijeva et al., 2020) has shown that a minority, yet significant number of pyrite grains analyzed contain measurable concentrations of invisible gold, thus warranting a study to determine the potential role and nature of invisible gold down to the nanoscale. We thus use complementary microanalytical techniques that bridge micron- to nanoscales of observation, to confirm that pyrite from the giant Olympic Dam Cu-U-Au-Ag deposit, South Australia, can, in some circumstances, host invisible gold. Our aims are to define the location and physical form of Au and accompanying elements. Although at concentrations below the solubility limit of gold in pyrite, our nanoscale approach reveals a complex evolution, in which trace elements are redistributed at the nanometer scale during superimposed brecciation of pyrite.

## Background

Olympic Dam is an archetypal iron-oxide copper gold (IOCG) deposit of Mesoproterozoic age exploited for Cu, U, Au, and Ag. The ore contains >100 minerals and features complex, finely intergrown sulfide assemblages (Ehrig et al., 2012; Ciobanu et al., 2017). Gold occurs in the Olympic Dam orebody at an average grade of 0.32 g/t but with significant variation between different parts of the deposit and rare 'bonanza' veins known from hematite-rich, gold-dominant zones (Ehrig et al., 2012). Gold occurs associated with sulfides but also within gold-dominant zones on the margins of barren hematite-quartz-baryte breccias without sulfides, and also within intensely altered granite breccias (Ehrig et al., 2017). Most gold in parts of the deposit explored in detail occurs as ~1 to 20 μm-sized native gold, and as subordinate petzite, calaverite and tetra-auricupride (Ehrig et al., 2012, 2017, Ciobanu, 2015). At Olympic Dam, Au is recovered via processing of copper anode slimes derived from smelting sulfide concentrates, and not via cyanide leaching of ore. Approximately 80% of the Au in the processing plant feed is recovered to the sulfide concentrate. This concentrate is then smelted to produce Cu-anodes, the anodes are electrorefined to produce Cu cathode. The anode slimes produced during Cu-refining are then subjected to a variety of leaches to ultimately produce Au and Ag bullion. Gold recovery from sulfide concentrates to gold bullion is ~96%.

126 Pyrite is a ubiquitous sulfide in some parts of the Olympic Dam deposit, particularly at deeper
127 levels and on the deposit margins, where it occurs together with chalcopyrite (Ehrig et al., 2012). The
128 potential contribution of invisible gold in pyrite to gold grades in pyrite-chalcopyrite ores from deeper
129 levels in the deposit has remained an open question until recently. Pyrite can be up to several
130 millimeters in size, with multiple textural types observed depending on assemblage; euhedral crystals
131 are, however, rare. Pyrite is often replaced by chalcopyrite but elsewhere appears co-genetic. Pyrite
132 may display compositional zoning and is an important host for As and Co. Zonal patterns are,
133 however, often deformed, patchy or absent, indicating complex histories of growth, resorption,
134 brecciation, recrystallization and aggregation.

135 New laser ablation inductively coupled plasma mass spectrometry (LA-ICP-MS) trace element
136 data for Olympic Dam pyrite from across the deposit has been given by Dmitrijeva et al. (2020). A
137 multivariate statistical approach on a large (4,926 analyses) dataset assisted definition of the
138 geochemical signature of the mineral in terms of a Ag-Bi-Pb-(Au) signature that infers the presence
139 of inclusions of discrete telluride phases and highly variable Co, Ni and As likely representing
140 oscillatory zoning. Pyrite, like other refractory minerals in the Olympic Dam ores (e.g., Fe-oxides:
141 Verdugo-Ihl et al., 2017, 2020; Ciobanu et al., 2019), thus carries a geochemical and textural signature
142 reflecting not only the primary characteristics of the ore-forming fluid and metal source at the time
143 of ore deposit formation, but also the impact of multi-stage overprinting, including cycles of partial
144 replacement and recrystallisation.

145 The study of Dmitrijeva et al. (2020) also revealed that some pyrites do contain gold at
146 concentrations measurable by LA-ICP-MS. This finding prompted the present study, on a
147 representative sample, to determine the nature of the invisible gold, and to assess whether micron- to
148 nanoscale observations may allow additional constraints to be placed on processes of gold
149 redistribution during events after initial deposit formation.

150 **Sample and methodology**

The studied sample (RX7684A) is representative of the pyrite-chalcopyrite orezone at Olympic Dam. Sulfides occur within a hematite breccia (Drillhole RD1988, 1806.6 m). The 1-metre interval assay (1806-1807 m) yielded 2.3 ppm Au. Pyrite is replaced, and typically enveloped by chalcopyrite. The sample contains abundant pyrite distributed throughout a matrix of Fe-oxides and other gangue minerals including sericite, quartz, fluorite and barite (Fig. 1). Initial inspection was undertaken in reflected light followed by imaging in backscatter mode on a FEI Quanta 450 scanning electron microscope, to identify suitable grains for LA-ICP-MS trace element analysis.

Two sets of LA-ICP-MS trace element data were collected (Online Material[1] Table 1). 163 spot analyses were made on 67 individual pyrite grains at the University of Tasmania, Hobart, Australia. These data were collected using a RESOlution-LR 193 nm ArF excimer laser with a large format S155 ablation cell, coupled to an Agilent 7500cs Quadrupole ICP-MS. Laser spot size varied from 19 to 33 μm. Isotopes measured were $^{27}$Al, $^{34}$S, $^{47}$Ti, $^{55}$Mn, $^{57}$Fe, $^{59}$Co, $^{60}$Ni, $^{65}$Cu, $^{66}$Zn, $^{75}$As, $^{77}$Se, $^{89}$Y, $^{90}$Zr, $^{95}$Mo, $^{109}$Ag, $^{111}$Cd, $^{118}$Sn, $^{121}$Sb, $^{125}$Te, $^{140}$Ce, $^{157}$Gd, $^{172}$Yb, $^{178}$Hf, $^{181}$Ta, $^{182}$W, $^{185}$Re, $^{197}$Au, $^{204}$Pb, $^{205}$Tl, $^{206}$Pb, $^{207}$Pb, $^{208}$Pb, $^{209}$Bi, $^{232}$Th, $^{235}$U and $^{238}$U.

Selected grains were re-analyzed using a RESOlution-LR 193 nm excimer laser microprobe (Australian Scientific Instruments) coupled to an Agilent 7900x Quadrupole ICP-MS (Adelaide Microscopy, The University of Adelaide). A laser spot size diameter of 29 μm was employed, using a pulse repetition rate of 5 Hz and a fluence of ~3 J/cm$^2$. Reference materials were run before and after sets of pyrite unknowns (typically less than 30 analyses), using STDGL3 and GSD-1G as the primary and secondary standards, respectively. Twenty-four isotopes, including four Pb isotopes, was measured: $^{34}$S, $^{55}$Mn, $^{57}$Fe, $^{59}$Co, $^{60}$Ni, $^{63}$Cu, $^{66}$Zn, $^{75}$As, $^{77}$Se, $^{95}$Mo, $^{107}$Ag, $^{111}$Cd, $^{118}$Sn, $^{121}$Sb, $^{125}$Te, $^{185}$Re, $^{197}$Au, $^{201}$Hg, $^{205}$Tl, $^{204}$Pb, $^{206}$Pb, $^{207}$Pb, $^{208}$Pb and $^{209}$Bi. Other isotopes, including $^{47}$Ti, $^{88}$Sr, $^{89}$Y, $^{90}$Zr, $^{137}$Ba, $^{140}$Ce, $^{157}$Gd, $^{172}$Yb, $^{178}$Hf, $^{182}$W, $^{232}$Th and $^{238}$U, were monitored to check for gangue inclusions. Reported Pb contents correspond to total Pb concentrations calculated from the individual abundances of $^{204}$Pb, $^{206}$Pb, $^{207}$Pb and $^{208}$Pb, correcting for radioactive decay of Th and U.

For both datasets, data reduction was performed in Iolite using Fe as the internal standard element, assuming the concentration in stoichiometric pyrite (46.551 wt.%). Detection limits were individually calculated for each element in each spot analysis based on the specific analytical conditions.

Statistical analysis was carried out on the combined LA-ICP-MS dataset by investigating the co-dependence between all possible pairs of elements using a variation matrix, calculating log-ratios $\tau_{ij}$ ($\tau_{ij}$ = variance) by the formula:

$$\tau_{ij} = \text{var}\left(\ln\frac{x_i}{x_j}\right),$$

where *i*, and *j* are indices for each element pair. Two multivariate statistical analysis methods, k-means clustering and Principal Component Analysis (PCA), were applied to the multi-element LA-ICP-MS dataset using 'R' statistical computing package and following procedures outlined in Dmitrijeva et al. (2020).

Four grains were selected for nanoscale investigation. Preparation of thinned (<100 nm) foils from the polished blocks for TEM investigation was performed using a FEI-Helios nanoLab Dual Focused Ion Beam Scanning Electron Microscope (FIB-SEM) at Adelaide Microscopy, The University of Adelaide, following procedures outlined by Ciobanu et al. (2011). Each TEM foil was attached to a copper grid.

Bright Field (BF) and high-angle annular dark field (HAADF) scanning transmission electron microscopy (STEM) imaging and STEM energy-dispersive spectrometry (EDS) spot analysis/mapping were performed using an ultra-high resolution, probe-corrected, FEI Titan Themis S/TEM operated at 200 kV. This instrument is equipped with the X-FEG Schottky source and Super-X EDS geometry. The Super-X STEM EDS detector provides geometrically symmetric EDS detection with an effective solid angle of 0.8 Sr. Probe correction delivered sub-Ångstrom spatial resolution, and an inner collection angle greater than 50 mrad was used for HAADF experiments using the Fischione HAADF detector. Diffraction measurements were performed using DigitalMicrographTM 3.11.1 software. Identification of zone axes was done using fast Fourier transform (FFT) obtained from images. Indexing of FFTs will be done using Winwulff' 1.5.2 software

and publicly available data from the American Mineralogist Crystal Structure Database. Crystal structure simulations were carried out using CrystalMaker 10.1.1and STEM for xHREM™ 4.1 software.

## Results

*Micron-scale characterization: Pyrite textures and geochemistry*

The analyzed sample is representative of Cu-Au-mineralized hematite breccias within the deeper chalcopyrite + pyrite zone within the south-eastern part of the Olympic Dam Breccia Complex (ODBC). Pyrite occurs as sub-mm sized grains that are apparently subhedral in morphology and display marginal replacement by chalcopyrite and a weak zoning observable in reflected light (Figs. 1b-e and 2a). We note scalloped boundaries against pyrite that are typical of replacement rather than overgrowth relationships between the two sulfides. These sulfide disseminations cluster along hematite clasts, which display brittle fracturing, marginal milling and grain rounding (Fig. 1f-h). Contemporaneous with these features, replacement of pyrite by chalcopyrite is supported by sulfide fabrics observed at the junctions between milled hematite clasts indicating ductile behavior of chalcopyrite during brecciation of pyrite and hematite; the latter contains magnetite as µm-sized inclusions (Fig. 1h). Most grains contain inclusions of gangue minerals and feature sub-micron-scale fractures and domains of abundant micropores. Internal zoning patterns with respect to the distributions of As, Co, and Ni (see below) reveal that each subhedral pyrite actually represents a reworked aggregate, in which individual sub-grains display oscillatory or patchy zonation patterns, disturbed to various degrees of reworking and partial resorption (Figs. 1i-k and 2b, c). Mutual boundaries between sub-grains are marked by the presence of pores, and sometimes, sub-micron inclusions of Au-, Ag-, Bi, and Te-bearing phases, as well as cassiterite and rare cobaltite (Fig. 2c, d). Such characteristics are typical of dissolution-reprecipitation boundaries within the studied pyrites. LA-ICP-MS trace element distribution maps (Fig. 2e, Online Material[1] Fig. A1) highlight the

[1] Deposit item

grain-scale heterogeneity but nevertheless also confirm that the zones enriched in As are also enriched with Au (often also Co, and sometimes Ni). In contrast, other elements, notably Bi and Te, are relatively enriched at sub-grain margins, or appear elevated in the enclosing chalcopyrite relative to pyrite (Online Material[2] Fig. A1).

LA-ICP-MS spot analysis yields concentrations of Au, As, Co and Ni that vary over several orders of magnitude and have maxima of 393, 34,000, 11,800, and 3,040 ppm, respectively. Silver, Bi, Cu, Pb, Se, Sn, and Te are also consistently measurable at concentrations well above minimum limits of detection. Full analyses are given in Online Material[1] Table A1.

Plotting the LA-ICP-MS dataset for Au-bearing pyrite on a scatterplot of Au *versus* As (Fig. 2f) shows that all data fall below the empirical solubility limit of Au in pyrite (Reich et al., 2005), inferring that Au should be in solid solution rather than present as nanoparticles. Moreover, representative time-resolved downhole LA-ICP-MS profiles for Au-rich domains (tens to hundreds of ppm) in pyrite are characterized by smooth signals for the measured isotopes (Fig. 2g), reinforcing such an interpretation.

*Statistical analysis*

The variation matrix (Online Material[1] Table A2) shows proportionality (small $\tau_{ij}$) and dissimilarity (large $\tau_{ij}$) among trace elements, as summarized on a cluster dendrogram (Fig. 3a). This shows two major groups of element associations: Group 1 comprising Mn, Ni, Zn, Co, Se and Te; and Group 2 consisting of Au, Sn, Cu, Bi, Pb, Sb, As and Ag. In general, the element associations identified on the dendrogram are verified by their geochemical affinities in the variation matrix (Online Material[1] Table A2). A high degree of association exists between the element pairs Au-As, Au-Ag, and Se-Te based on relatively low $\tau_{ij}$ values. The element pairs Co-Au, Ni-Au, Se-Au, and Te-Au display large $\tau_{ij}$ and have the lowest correlation.

[2] Deposit item

In contrast to the two groups shown on the dendrogram, three optimal clusters were identified by k-means cluster analysis: (1) Au-As poor (81 analyses); (2) Au-As-rich (43 analyses); and (3) Au-As-Sn rich (39 analyses). A boxplot comparing the three k-clusters (Fig. 3b) shows the clusters are discriminated by greater variation in Sn and Au, but barely distinguishable in terms of Ni. The three clusters are also depicted by PCA analysis (Fig. 3c) and the correlation between elements visualized as PC loadings (Fig. 3d). A 180-degree angle between two vectors implies a negative correlation (e.g Au vs Co) whereas a strong correlation is suggested by a small angle. For example, on the PC1-PC2 projection (Fig. 3d), Au and As show a strong correlation, as well as a relatively good association with elements from Group 2 (Bi, Pb, Sb, and Ag). In contrast, the roughly orthogonal angle between the two vectors shows a lesser association between Au and Sn and the 180-degree angle between Au and Co suggests a lack of Au wherever Co is present. On the other hand, a good association is recognizable on Fig. 3d between Group 1 elements (Te, Se, Co, and Ni).

*Textures and trace element distributions at the nanoscale*

The nanoscale study addressed boundary domains between sub-grains within four foils (Fig. 4), which were prepared from two pyrites with high concentrations of Au and As (yellow circles on Fig. 2f). In addition, two other foils were extracted from: (i) pyrite that show micron-sized Bi-telluride inclusions at the boundary to chalcopyrite (pyrite grain 57; foil #5), and (ii) unzoned, Au-As-poor pyrite (pyrite 37; foil #6) (Online Material[1] Fig. A2a-e).

Low-resolution imaging of the four foils obtained from grain boundaries shows faint zonation patterns, and cross-cutting microstructures that are recognizable by their relative brightness or higher HAADF signal intensity (hereafter called splays). STEM EDS element mapping of domains within the foils reveals the fine-scale nature of crystal growth zoning with respect to As, Co and Ni, as well as further details along mutual intra-grain boundaries (Fig. 5). The pyrite displaying high porosity and reshaping of zonation on the surface (Py37; foil #1; Fig. 2c) preserves an area with oscillatory compositional zoning (Fig. 5a) that mimics the rhythmic banding observed at surface (BSE image in Fig. 2c). In this case, the zoning features relatively broad bands, hundreds of nm across, that are

enriched in As, Ni (and lesser Co) separated by narrower, As-only bands without Ni or Co (Fig. 5a). Crosscutting sets of splays are observed, some of which host fine particles (inclusions up to ~1 μm in size), which do not correlate with As or Ni enrichment (Fig. 5). The three grain boundaries from the other studied pyrite aggregate (Py67a; foils #2-4) display different patterns picked out on the element maps by the distributions of As and Co (Fig. 5b-d). An unzoned, As-rich grain outlined by Co-rich fringes (Fig. 5b) is present immediately underneath the surface along boundary 1 (Fig. 2b). Fine-scale rhythmic zonation (Fig. 5c, d) and superimposed (new) grains are depicted by the distributions of As and Co across the other two boundaries in the same aggregate (Fig. 4b). Variation in the concentrations of As and Co reveals a reworking of earlier heterogeneity into a still finer, patchy banding accompanied by nucleation of discrete Co- and As-rich inclusions as fine particles of cobaltite, CoAsS, and/or safflorite, $(Co,Fe)As_2$ (Fig. 5c). New growth of As-rich pyrite at the contact between pre-existing pyrite sub-grains, each with distinct zonation patterns, is outlined by Co-rich fringes that host arrays of cobaltite nanoparticles up to 100 nm in size (Fig. 5d).

HAADF and BF STEM imaging reveals a diverse range of micro- and nanostructures in pyrite which are associated with presence of mineral inclusions (Figs. 6 and 7) and these areas were targeted for STEM EDS element mapping at higher resolution (see below). Grain boundaries are crosscut by duplex-dipole structures (a dipole is defined by paired traces of darker color on BF images; Fig. 6a). Such structures have also a slightly modified/distinct composition to the host assemblage as they appear as faint-brighter traces (splays) on the HAADF image (Fig. 6b). Zonation patterns are crosscut by duplex and/or sets of quasi-parallel splays that represent the largest, planar microstructures (hundreds of $nm^2$ in size) observed throughout all foils (Fig. 6a, b). Such wider microstructures are of particular relevance for the nanoscale remobilization of trace elements that accompanies the nucleation of inclusions, often at junctions of several splays (Figs. 4a and 6b). When imaged at higher resolution, the quasi-parallel splays are seen as microstructures formed by bands (5-20 nm in width) of rhythmic misorientation to one another (Fig. 6c).

HAADF STEM imaging shows an eclectic range of nanomineral inclusions of variable sizes and morphology which are associated with pores and/or splays displaying patterns that are neither as wide or as regular as the fields of rhythmic misorientation structures (Fig. 6d-i). The speciation of inclusions and their association with Au-bearing NPs differs between the two studied pyrites (see also below). Electrum is found as the smallest NPs, no more than a few nm in diameter, hosted by larger particles of chalcopyrite and the Bi-Ag-telluride volynskite ($AgBiTe_2$) only in foil #1 from Py37 (Fig. 6d, e). These particles have globular morphology and are associated with nanopores. Electrum occurs close to a nanopore enclosed in chalcopyrite (Fig. 6d) whereas the Bi-Ag-telluride and electrum are either attached to, or coat, a larger cavity linked to an array of small Bi-bearing NPs (Fig. 6e). The most common type of nanomineral inclusions throughout all examined foils are Bi-Pb-Te-bearing particles, some of which can reach tens of nm, and rarely even hundreds of nm in size (Fig. 6f-h). In such cases they have angular morphology and are associated with irregular splays along scalloped boundaries between domains of pyrite zoned with respect to As and Co and unzoned pyrite (Fig. 6f), at junctions between such splays with either chaotic or quasi-parallel distribution (Fig.6g, h). This class of inclusions are either Bi-Pb-sulfotellurides belonging to the aleksite series (Cook et al., 2007, 2019) or, more rarely, Bi-Ag-Te-bearing galena (see also below). In contrast, speciation of tellurides changes for inclusions at the margin of pyrite, at the contact with chalcopyrite (Py57), whereby µm-sized tellurobismuthite ($Bi_2Te_3$) and altaite (PbTe) are present (Online Material[1] Fig. A2f, g). Euhedral, nanoinclusions of cassiterite of varying size are also widespread throughout all foils (Fig. 6i; Online Material[1] Fig. A2e), albeit never as abundant as the Bi-Pb-sulfotellurides.

The grain boundaries in Py67a (foils #2-4) are typified by abundant nanostructures controlling (re)-mobilization of precious metals and accompanying trace elements (Bi, Pb, Te), collectively resulting in a strong association between Bi-Pb-sulfotelluride and Au-Ag-telluride NPs (Fig. 6j, k). Such nanostructures consist of finest splays, only a few nm in width, forming swarms or parallel arrays that can extend over lengths of several hundred nm, along which trails of tiny telluride NPs occur (Fig. 6j). In contrast to the Au-Ag-Te-enrichment that occurs as discrete NPs, the Bi-Pb-Te-

326 association can be traced from areas of faint enrichment to clustered Bi-Pb-sulfotelluride NPs within
327 the nanostructures (Fig. 6k).

328 Structural characterization of splays described above as nanoscale structures was constrained from
329 BF STEM imaging of foils #2-4 by tilting the pyrite on several main zone axes (Fig. 7). Dislocation
330 planes were identified along the dissolution-reprecipitation boundaries on [100] and [1-10] zone axes
331 (Fig. 7a-c). These consist of dipoles with apex loops at crystal edges growing along <011> directions
332 (Fig. 7b). Cobaltite inclusions occur at dissolution boundaries with kinked <111>/<100> trajectory
333 (Fig. 7c). Such kinks are also marked by loops comprising *en-echelon* microcracks (Fig. 7c) along
334 which inclusion nucleation takes place. The majority of Au-Ag and Bi-Te-nanoparticles are found
335 within finest nanostructures further away from the dissolution-reprecipitation boundaries.
336 Nanoparticles are hosted within loops at the apex of single, duplex or radial dipoles imaged on [-112]
337 zone axis in pyrite (Fig. 7d-f). Nucleation occurs also at locations showing twists and changes in
338 dipole orientation from <0-21> to <111> directions, whereas clustered NPs form at the edges of radial
339 dipoles (Fig. 7d-f).

340 A complex array of dislocations associated with particle nucleation (named dislocation nucleation)
341 can occur in the same domain (several hundred $nm^2$) in pyrite imaged on [1-10] zone axis (Fig. 7g-
342 i). Enrichment in Bi, Pb and Te occurs as well-defined lamella of Bi-Pb-sulfotellurides at dislocation
343 junctions (Fig. 7g) or as a smearing of these elements at twist-wall boundaries (Fig. 7h). Coarser, fine
344 particles of Fe-oxides (most likely hematite) are surrounded by radial dislocations (Fig. 7i).

345 Nanoparticles associated with dislocation nucleation on slip planes in pyrite were imaged on [-
346 110], [-112] and [100] zone axes in pyrite (Fig. 7j-m). Typical structures along <100> directions,
347 with secondary <111> branches, show *en-echelon* <311> oriented arrays with dislocation tilt (Fig.
348 7j). Conjugate <201>/<02-1> slip systems host NPs at plane junctions (Fig. 7k), Gold-Ag-tellurides
349 NPs are abundant along *en-echelon* dislocations and particularly on low-angle slip systems (Fig. 7l,
350 m).

Trace element remobilization at the nanoscale is documented from high resolution STEM EDS maps (Fig. 8, Online Material[1] Fig. A3). Recognizable concentrations of Bi, Pb, Ag and Te can be mapped as thin lines that trail away from galena NPs (Fig. 8a). Notable, however, are the relative differences in element mobility, as for example high for Bi and lower for Pb, Te and Ag. The narrowest planes within the nanostructures, 1-2 nm in width, are traceable by Bi, Pb and Te, as well as slightly wider haloes of Co (Fig. 8b), the latter is accompanied by As. Likewise, splays enriched in Co and As are mapped in areas with Au-Ag-telluride or B-Pb-sulfotellurides NPs (Fig. 8c; Online Material[1] Fig. A3a).

High-resolution STEM EDS mapping and integrated spectra/spot analysis were carried out to identify the composition of NPs and their associations (Fig. 9; Online Material[1] Fig. A3). The smallest electrum NPs are found attached to pores in chalcopyrite whereas the largest occurrence of electrum consists of several NPs harbored within an agglomeration of Bi-Ag-telluride NPs (Fig. 9a-c). Petzite ($Ag_3AuTe_2$), forming single or multicomponent NPs with sylvanite [$(Au,Ag)Te_2$] and Bi-Pb-sulfotellurides are the most common NPs identified (Fig. 9d; Online Material[1] Fig. A2a). Note that these NPs often show Co (As)-enriched tails. The layered structure of the Bi-Pb-sulfotellurides is reproduced on the maps by correlation between Bi-Te and Pb-S rich bands (Fig. 9e). Cassiterite NPs from the unzoned pyrite (foil #6) display instead marginal haloes of Te- and Cl-Na-enrichment (Fig. 9f).

*High-resolution imaging: phase identification*

High-resolution imaging was undertaken to: (i) characterize pyrite on zone axes that are typical of either *Pa*3 cubic or *P*-1 triclinic symmetry (Bayliss, 1977); (ii) assess the presence of defects and/or phase transformations that allow trace element remobilization and formation of NPs; and (iii) identify speciation of tellurides.

Pyrite was imaged on four main zone axes (Online Material[1] Fig. A4). Fast Fourier transform (FFT) patterns obtained from the images were indexed and compared with simulated Selected Area Electron Diffractions (SAED), STEM simulations and crystal models, with a good match between

data and simulations. Indexing was done using the *P*-1 instead of *Pa*3 space group obtained for weakly anisotropic pyrite (Bayliss, 1977).

Atomic-scale imaging of defects associated with trace element (re)mobilization provides further insights into inclusion nucleation in pyrite (#67a; Fig. 10). Slip planes along <02-1> directions in pyrite show atom dislocation perpendicular to plane traces that display relative enrichment in Bi, Pb, and Te (Fig. 10a, b). However, nucleation of nm-wide lamellae of Bi-Pb-sulfotellurides (Fig. 10c, d) takes place along kinked dipoles, as those shown in Figure 7d, with smearing of heavy elements (Bi, Pb, and Te) at the junction between planes. In contrast with such structures, single planes with screw dislocation along <100> directions in pyrite are not associated with inclusion nucleation (Fig. 10e-g). Edge and screw dislocations along slip planes (Fig. 10g) nonetheless provide sites for fluid percolation, thus assisting inclusion nucleation. For example, the contacts between domains with different step-overs marked by bright strips (Fig. 10e, f). Although such screw dislocation defects may account for 'marcasitization' (e.g., Posfai and Buseck, 1997), or loss of S (formation of pyrrhotite), such phenomena cannot be constrained based on the present data.

Several inclusions of Au-Ag- and Bi-Pb-sulfotellurides were suitable for imaging at atomic-scale resolution (Fig. 11). Petzite and sylvanite form coherent intergrowths with one another and also with host pyrite (Fig. 11a, b). Petzite is confirmed from the imaging and FFT pattern on [-111] zone axis (Fig. 11b). Whereas the two Au-Ag-tellurides described here clearly have different Au-Ag ratios, the Au-rich species is difficult to distinguish from the petzite based on STEM EDS spectra considering their partial spatial overlap. This is not surprising considering the close similarity between the crystal structures of several species in the system Au-Ag-Te (Bindi, 2008, and references therein). Ideal sylvanite has the commensurate modulated superstructure of calaverite but non-stoichiometry induces periodic displacements and periodic antiphase boundaries (van Tendeloo et al., 1983, 1984). The small size of the inclusion discussed here hampers further insight into the crystal structural modularity.

Bismuth-Pb-sulfotellurides form the aleksite series with phases derived from the tetradymite archetype, known as the '5-atom' (Te-Bi-S-Bi-Te) layer (Cook et al., 2007). These are mixed-layer compounds in which discrete compositional changes are accommodated by stacking sequences with odd-number of atom layers, 7-, 9-, 11-, etc. The arrangement of these layers is depicted on electron diffraction patterns (Ciobanu et al., 2009) and the layer stacking can be used to calculate their composition (Cook et al., 2019). For example, the composition of the Bi-Pb-sulfotelluride inclusion in Figure 11c can be calculated from the layer stacking as $PbBi_4Te_4S_3$, which was recently shown (Cook et al., 2019) to exist as several polytypic sequences among which the simplest is the '57' repeat. The present inclusion is, however, highly disordered with no regular layer repeat. The width of the layers (L) can be easily visualized on HAADF STEM images (Fig. 11d) and calculated as: L= n + m, where n =number of bright atoms (Bi, Pb) and m=number of chalcogen (S, Te), m=n+1.

## Discussion

*Trace elements (re)mobilization during pyrite deformation at the brittle to ductile transition*

The correlation between micron- and nanoscale zonation patterns within Au-bearing pyrite, e.g., the overlap between As, Co and Ni on the LA-ICP-MS element maps, is reproduced at the nanoscale within distinct bands (compare maps in Fig. 5a and Online Material[1] Fig. A1). This indicates preservation of an initial cycle of growth typified by oscillatory zoning. The present study illustrates the ultrafine-scale of that compositional banding (Fig. 5c, d), well below the spatial resolution achievable when mapping by LA-ICP-MS. Compounding this, the low Au concentrations measured by LA-ICP-MS spot analysis, never more than tens or a few hundred ppm, are well below the threshold of the STEM EDS detectors and could not be measured or mapped with the present instrument configuration.

Patterns and textures at the µm-scale such as porosity, sub-µm-sized inclusions, or fracturing, all of which are associated with a reshaping of the primary zoning (Figs. 2a-c and 4a, b), infer overprinting via interaction with fluids. The abundance of micro- and nanostructures, e.g., dipoles,

dislocations, or dissolution-reprecipitation boundaries (Figs. 6 and 7) indicate that trace element redistribution in pyrite took place under strain induced by an oriented stress event postdating initial crystallization. Although not always associated with chemical patterning, our assumption of oriented stress impacting on pyrite is also supported by the presence of rhythmic misorientation textures (Fig. 6c) that resemble μm-scale misorientation fabrics unrelated to compositional heterogeneity which have been documented from EBSD studies of pyrite that underwent syn-metamorphic plastic deformation (Boyle et al., 1998; Barrie et al., 2008, 2010a, 2010b). Low-angle slip dislocations, twist walls and deformation-dipole nanostructures (Fig. 7) indicate brittle-to-ductile deformation of pyrite at P-T conditions attainable during brecciation in the deeper parts of the deposit. These conditions can be estimated at 0.5-1 kbar and 300-400 °C based on current models for the mineralizing event at Olympic Dam (Courtney-Davies et al., 2020; Verdugo-Ihl et al., 2020).

Considering the brittle-to-ductile regime during pyrite reworking, recrystallization of brecciated grains (e.g., Py67a; Figs. 2a, b and 4b, d-f) can be considered as intragrain annealing. At this stage, decoupling between As, Co and Ni takes place, as documented from our mapping at the nanoscale (Fig. 5b-d). This suggests that Ni is most likely preferentially incorporated into fluid and (re)precipitated into other pyrites (e.g., grain that are Ni-Co-rich but As, Au-poor Online Material1 Figure A1d). Whereas Co and As are retained within overprinting (nano)structures during further textural reworking, Ni is either dissipated, diminished, or lost altogether (Fig. 5c, d). In the same case, the reworking of pyrite via processes that preserve and recycle elements that are already present within the pyrite is evidenced by new growth of distinct grains along annealed boundaries that are As-rich yet lack oscillatory zoning (Fig. 5b). Advanced porosity, mosaic-dissolution boundaries and infill by chalcopyrite show that some grains have experienced more intense fluid percolation at some point following the annealing episode (Py37; Figs. 2c, d and 4a, c). Such fluids are clearly fingerprinted by a coating of NaCl on some of the cassiterite NPs (Fig. 9f).

*Lifting the cloak of invisibility – where is the gold in pyrite?*

Neither the "arsenic-driven pump for invisible gold in hydrothermal systems" (Pokrovski et al., 2021) nor a mechanism of Au-nanoparticles forming upon supersaturation from an As-rich pyrite (Reich et al., 2005; Deditius et al., 2014) can fully explain the present data which lie within the solid solution domain for pyrite when plotted in terms of Au vs. As concentration (Fig. 2f).

Our study shows that Au-bearing nanoparticles are tied to reworking of pyrite both during and following brecciation events. This is, to some extent, consistent with prior studies showing scenarios for the occurrence of 'invisible Au' in pyrite, particularly in orogenic Au deposits, that lie outside or contradict the paradigm of "coupled geochemical behavior of Au and As" (Deditius et al., 2014). Among these is the exceptional case of As-free pyrite containing up to several thousand ppm Au, in which nanoparticles of Au-Ag-tellurides are tied to brecciated domains formed during a devolatilization event (Cook et al., 2009; Ciobanu et al., 2011, 2012). Likewise, atom-cluster enrichment in Au, Ni, Cu, and Bi has been imaged by atom probe tomography (APT) along dislocations hosted in a deformation low-angle boundary in pyrite (Fougerouse et al., 2021). Also, directly relevant here, is the model for "retrograde As contents of hydrothermal pyrite", which considers that As- and Au-enrichment in pyrite occurs during prolonged fluid-interaction, often the case of orogenic Au deposits (e.g., Sung et al., 2009), and without the requirement of any anomalously Au-rich fluid (Xing et al., 2019).

We show that gold is linked to nanostructures of which the smallest are nm-wide pathways in pyrite that can be recognized from their characteristic enrichment in a diverse trace element association (Fig. 8, Online Material[1] Fig. A3). Dislocation planes associated with splays of various orientation relative to primary or secondary zonation promote the migration and/or infiltration of trace elements and, subsequently, as permeability becomes restricted, to nucleation of inclusions (Fig. 9). Analogous aspects were reported for arsenopyrite based on EBSD data and SIMS mapping (Fougerouse et al., 2016a). Although Co and As also occur along such defects in pyrite, there is a far stronger correlation between Au-bearing NPs and elements contained within the Bi-(Pb)-chalcogenides than with the products of As-, Co-(re)mobilization. The extent of such processes is

478 highlighted by the abundance of NPs tied to planes enriched in chalcogens (notably Te) and
479 chalcophile elements (Bi, Pb, Ag) forming Bi-chalcogenide inclusions in the annealed pyrite (Fig.
480 10). Chalcogenides of bismuth and other metals are widely reported as accessory phases in gold ores
481 of different genetic types and have been postulated to make a significant contribution to Au
482 enrichment in ores, particularly if conditions facilitate the so-called "Bi-melt scavenger for Au"
483 mechanism (e.g., Meinert, 2000; Tomkins and Mavrogenes, 2002; Ciobanu et al., 2005, 2006, 2010;
484 Törmänen and Koski, 2005).

485 It has been shown, both by modelling of equilibrium thermodynamics and from experiments
486 involving dissolution-reprecipitation reactions (Tooth et al., 2008, 2011), that Bi-rich melts can
487 efficiently scavenge Au from hydrothermal fluids that are undersaturated with respect to Au.
488 Moreover, the products of such melts can precipitate as Bi-bearing mineral associations within pores
489 created by the advance of the interface coupled dissolution reaction (Tooth et al., 2011). Such a
490 scenario plausibly explains formation of Bi-Ag- and Au-bearing NPs coating pores in the sample with
491 higher fluid rates of percolation (Fig. 6e).

492 The present data shows that the pattern of gold distribution and geochemical clustering in pyrite
493 from a single sample (Fig. 3) strongly mirrors that identified by statistical analysis of much larger
494 datasets for Olympic Dam pyrite (Dmitrijeva et al., 2020). The discovery of nanoscale Bi-, Au-(Ag)-
495 tellurides, Bi-Pb-sulfotellurides and cassiterite backs up the prediction of such phases within Olympic
496 Dam pyrite (Dmitrijeva et al., 2020). We speculate that Au, Te, and Bi were sourced from the pyrite
497 itself, whereas Pb and Sn were supplied from the breakdown of hematite that forms the breccia matrix
498 (Fig. 1). These elements are part of a characteristic hematite signature (U-Pb-W-Sn-Mo) identified
499 throughout the Olympic Dam deposit (Verdugo-Ihl et al., 2017). Release of radiogenic Pb from
500 hematite, and implicitly, decoupling from parent U (Courtney-Davies et al., 2019) leads to isotopic
501 signatures that may preclude meaningful Pb-Pb dating of pyrite. Migration of radiogenic Pb into
502 boundaries between sulfide sub-grains at Olympic Dam is documented from nanoSIMS isotope
503 mapping coupled with EBSD analysis (Rollog et al., 2020). A preservation of discrete nanometer-

scale Pb reservoirs of various isotopic compositions within grain boundaries acting as open systems over 1 billion years after pyrite formation is likely, analogous to that shown by APT studies of Witwatersrand pyrite (Fougerouse et al., 2019).

## Implications

The ever-increasing resolution and sensitivity achievable with contemporary microanalytical techniques reveals new layers of complexity with respect to the incorporation of trace/minor elements in a mineral matrix and their subsequent release in response to superimposed events. The present contribution highlights how the presence of Au and associated trace elements in pyrite can be related to strain-induced nanoscale structures formed during superimposed brecciation. Whereas the pyrite characterized here is As-bearing, Au-NP formation is decoupled from initial incorporation of As, instead fingerprinting pathways of enrichment and remobilization in Te, Bi, and Pb, elements which can otherwise be present at concentrations as low as Au in host pyrite or adjacent host minerals. Such pyrite is likely not only a feature of ancient IOCG deposits but could occur in any deposit formed over a protracted geological timescale. Linking micron- to nanoscale observations, we show that pyrites, no more than several mm apart, record textures indicating variation in the rates of percolation and strain achievable during fluid-mineral interaction, in which short-term permeability can explain the sequestration of new phases within the reaction areas themselves rather than outside of the pyrite.

The presence of invisible gold at Olympic Dam carries only limited implications for gold recovery as the pyrite reports to copper concentrates and is subsequently smelted, with gold recovery taking place during the processing of anode slimes, post electrorefining of copper anodes. Our results are, however, significant for constraining the hosts for chalcogens in mill feed, particularly those considered as ‘critical minerals’, notably Te, which is also concentrated in anode slimes.

## Acknowledgements

We acknowledge funding through Australian Research Council Linkage grant LP200100156 (Critical Minerals from Complex Ores). Preliminary work was undertaken by Hons. students Quang Minh Bui and Jiahe

Chen. Paul Olin (CODES, University of Tasmania) and Sarah Gilbert (University of Adelaide) assisted with LA-ICPMS analysis. Constructive comments from referees Denis Fougerouse and Artur Deditius helped us improve this manuscript. We appreciate expert handling by Associate Editor Daniel Gregory.

## References

Amodeo, J., Merkel, S., Tromas, C., Carrez, P., Korte-Kerzel, S., Cordier, P., and Chevalier, J. (2018) Dislocations and Plastic Deformation in MgO Crystals: A Review. Crystals, 8, 1-53.

Barrie, C.D., Boyle, A.P., Cox, S.F., and Prior, D.J. (2008) Slip systems and critical resolved shear stress in pyrite: an electron backscatter diffraction (EBSD) investigation. Mineralogical Magazine

Barrie, C.D., Boyle, A.P., and Salter, M. (2009) How low can you go? - Extending downwards the limits of plastic deformation in pyrite. Mineralogical Magazine, 73, 895-913.

Barrie, C.D., Boyle, A.P., Cook, N.J., and Prior, D.J. (2010a) Pyrite deformation textures in the massive sulfide ore deposits of the Norwegian Caledonides. Tectonophysics, 483, 269-286.

Barrie, C.D., Cook, N.J., and Boyle, A.P. (2010b) Textural variation in the pyrite-rich ore deposits of the Røros district, Trondheim Region, Norway: implications for pyrite deformation mechanisms. Mineralium Deposita, 45, 51–68.

Barrie, C.D., Pearce, M.A., and Boyle, A.P. (2011) Reconstructing the pyrite deformation mechanism map. Ore Geology Reviews, 39, 265-276.

Bayliss, P. (1977) Crystal structure refinement of a weakly anisotropic pyrite. American Mineralogist, 62, 1168-1172.

Bindi, L. (2008) Commensurate-incommensurate phase transition in muthmannite, $AuAgTe_2$: first evidence of a modulated structure at low temperature: Philosophical Magazine Letters, 88, 533–541.

Boyle, A.P., Prior, D.J., Banham, M.H., and Timms, N.E. (1998) Plastic deformation of metamorphic pyrite. new evidence from electron backscatter diffraction and forescatter orientation contrast imaging. Mineralium Deposita, 34, 71–81.

Ciobanu, C.L. (2015) Trace element signatures in sulfides from Olympic Dam and adjacent prospects: Unpublished report for BHP Olympic Dam, 400 pp.

Ciobanu, C.L., Cook, N.J., and Pring, A. (2005) Bismuth tellurides as gold scavengers. In: Mao, J.W., and Bierlein, F.P., eds., Mineral Deposit Research: Meeting the Global Challenge: Berlin, Heidelberg, New York, Springer, p. 1387–1390.

Ciobanu, C.L., Cook, N.J., Damian, F., and Damian, G. (2006) Gold scavenged by bismuth melts: an example from Alpine shear-remobilisates in the Highiş Massif, Romania. Mineralogy and Petrology, 87, 351–384.

Ciobanu, C.L., Pring, A., Cook, N.J., Self, P., Jefferson, D., Dima, G.I., and Melnikov, V. (2009) Chemical-structural modularity in the tetradymite group: A HRTEM study. American Mineralogist, 94, 517–534.

Ciobanu, C.L., Birch, W.D., Cook, N.J., Pring, A., and Grundler, P.V. (2010) Petrogenetic significance of Au–Bi–Te–S associations: the example of Maldon, Central Victorian gold province, Australia. Lithos, 116, 1–17.

Ciobanu, C.L., Cook, N.J., Utsunomiya, S., Pring, A., and Green, L. (2011) Focussed ion beam–transmission electron microscopy applications in ore mineralogy: Bridging micro- and nanoscale observations. Ore Geology Reviews, 42, 6-31.

Ciobanu, C.L., Cook, N.J., Utsunomiya, S., Kogagwa, M., Green, L., Gilbert, S., and Wade, B. (2012) Gold-telluride nanoparticles revealed in arsenic-free pyrite. American Mineralogist, 97, 1515-1518.

Ciobanu, C.L., Cook, N.J., and Ehrig, K. (2017) Ore minerals down to the nanoscale: Cu-(Fe)-sulphides from the iron oxide copper gold deposit at Olympic Dam, South Australia. Ore Geology Reviews, 81, 1218-1235.

Ciobanu, C.L., Verdugo-Ihl, M.R., Slattery, A., Cook, N.J., Ehrig, K., Courtney-Davies, L., and Wade, B.P. (2019) Silician Magnetite: Si–Fe-Nanoprecipitates and Other Mineral Inclusions in Magnetite from the Olympic Dam Deposit, South Australia. Minerals, 9, 311.

Cook, N.J., and Chryssoulis, S.L. (1990) Concentrations of "invisible gold" in the common sulphides. Canadian Mineralogist, 28, 1-16.

Cook, N.J., Ciobanu, C.L., Stanley, C.J., Paar, W., and Sundblad, K. (2007) Compositional data for Bi-Pb tellurosulfides. Canadian Mineralogist, 45, 417–435.

Cook, N.J., Ciobanu, C.L., and Mao, J. (2009) Textural control on gold distribution in As-free pyrite from the Dongping, Huangtuliang and Hougou gold deposits, North China Craton (Hebei Province, China). Chemical Geology, 264, 101-121.

Cook, N.J., Ciobanu, C.L., Meria, D., Silcock, D., and Wade, B. (2013) Arsenopyrite-Pyrite Association in an Orogenic Gold Ore: Tracing Mineralization History from Textures and Trace Elements, Economic Geology, 108, 1273-1283.

Cook, N.J., Ciobanu, C.L., Liu, W.Y., Slattery, A., Wade, B.P., Mills, S., and Stanley, C.J. (2019) Polytypism and polysomatism in mixed-layer chalcogenides: characterization of $PbBi_4Te_4S_3$ and inferences for ordered phases in the aleksite series. Minerals, 9, 628.

Couderc, J. J., Bras, J., Fagot, M., and Levade, C. (1980) Étude par microscopie ectroniquen transmission de l'état de déformation de pyrites de différentes provenances: Bulletin de Mineralogie, 105, 547-557.

Courtney-Davies, L., Tapster, S.R., Ciobanu, C.L., Cook, N.J., Verdugo-Ihl, M.R., Ehrig, K.J., Kennedy, A.K., Gilbert, S.E., Condon, D.J., and Wade, B.P. (2019) A multi-technique evaluation of hydrothermal hematite U-Pb isotope systematics: Implications for ore deposit geochronology. Chemical Geology, 513, 54-72.

Courtney-Davies, L., Ciobanu, C.L., Tapster, S.R., Cook, N.J., Ehrig, K., Crowley, J.L., Verdugo-Ihl, M.R., Wade, B.P., and Condon, D.J. (2020) Opening the Magmatic-Hydrothermal Window: High-Precision U-Pb Geochronology of the Mesoproterozoic Olympic Dam Cu-U-Au-Ag Deposit, South Australia. Economic Geology, 115, 1855-1870.

Cox, S.F. (1987) Flow mechanisms in sulphide minerals. Ore Geology Reviews, 2, 133–171.

Cox, S.F., Etheridge, M.A., and Hobbs, B.E. (1981) The experimental ductile deformation of polycrystalline and single-crystal pyrite. Economic Geology, 76, 2105–2117.

Deditius, A.P., Utsunomiya, S., Renock, D., Ewing, R.C., Ramana, C.V., Becker, U., and Kesler, S.E. (2008) A proposed new type of arsenian pyrite: composition, nanostructure and geological significance. Geochimica et Cosmochimica Acta, 72, 2919-2933.

Deditius, A.P., Reich, M., Kesler, S.E., Utsunomiya, S., Chryssoulis, S.L., Walshe, J., and Ewing, R.C. (2014) The coupled geochemistry of Au and As in pyrite from hydrothermal ore deposits. Geochimica et Cosmochimica Acta, 140, 644-670.

Dmitrijeva, M., Cook, N.J., Ehrig, K., Ciobanu, C.L., Metcalfe, A.V., Kamenetsky, M., Kamenetsky, V.S., and Gilbert, S.E. (2020) Multivariate statistical analysis of trace elements in pyrite: prediction, bias and artefacts in defining mineral signatures. Minerals, 10, 61.

Ehrig, K., McPhie, J., and Kamenetsky, V. (2012) Geology and mineralogical zonation of the Olympic Dam iron oxide Cu-U-Au-Ag deposit, South Australia. In: Hedenquist, J.W., Harris, M., Camus, F. (Eds), Geology and Genesis of Major Copper Deposits and Districts of the World, a Tribute to Richard Sillitoe. SEG Special Publication, 16, p. 237-268.

Ehrig, K., Kamenetsky, V., Mc`Phie, J., Cook, N.J., and Ciobanu, C.L. (2017) Olympic Dam iron-oxide Cu-U-Au-Ag deposit. In: G.N. Phillips (Ed.), Australian Ore Deposits. AusIMM, Melbourne, p. 601-610.

Fougerouse, D., Micklethwaite, S., Halfpenny, A., Reddy, S.M., Cliff, J.B., Martin, L.A., Kilburn, M., Guagliardo, P., and Ulrich, S. (2016a) The golden ark: arsenopyrite crystal plasticity and the retention of gold through high strain and metamorphism. Terra Nova, 28, 181-187.

Fougerouse, D., Reddy, S.M., Saxey, D.W., Rickard, W.D.A., van Riessen, A., and Micklethwaite, S. (2016b) Nanoscale gold clusters in arsenopyrite controlled by growth rate not concentration: evidence from atom probe microscopy. American Mineralogist, 101, 1916-1919.

Fougerouse, D., Reddy, S.M., Kirkland, C.L., Saxey, D.W., Rickard, W.D., and Hough, R.M. (2019) Time-resolved, defect-hosted, trace element mobility in deformed Witwatersrand pyrite: Geoscience Frontiers, 10, 55–63.

Fougerouse, D., Reddy, S.M., Aylmore, M., Yang, L., Guagliardo, P., Saxey, D.W., Rickard, W.D.A., and Timms, N. (2021) A new kind of invisible gold in pyrite hosted in deformation-related dislocations. Geology, 49, 1225–1229.

Freitag, K., Boyle, A.P., Nelson, E., Hitzman, M., Churchill, J., and Lopez-Pedrosa, M. (2004) The use of electron backscatter diffraction and orientation contrast imaging as tools for sulphide textural studies: example from the Greens Creek deposit (Alaska). Mineralium Deposita, 39, 103-113.

Gong, M., Kirkeminde, A., and Ren, S. (2013) Symmetry-Defying Iron Pyrite ($FeS_2$) Nanocrystals through Oriented Attachment. Scientific Reports, 3, 2092; DOI: 10.1038/srep02092.

Graf, J.L., Skinner, B.J., Bras, J., Fagot, M., Levade, C., and Couderc, J.J. (1981) Transmission electron-microscopic observation of plastic deformation in experimentally deformed pyrite. Economic Geology, 76, 738–742.

Gregory, D.D., Large, R.R., Halpin, J.A., Baturina, E.L., Lyons, T.W., Wu, S., Danyushevsky, L., Sack, P.J., Chappaz, A., and Maslennikov, V.V. (2015) Trace element content of sedimentary pyrite in black shales: Economic Geology, 110, 1389-1410.

Large, R.R., Danyushevsky, L., Hollit, C., Maslennikov, V., Meffre, S., Gilbert, S., Singh, B., Scott, R., Emsbo, P., Thomas, H., Singn, B., and Foster, J. (2009) Gold and trace element zonation in pyrite using a laser imaging technique: Implications for the timing of gold in orogenic and Carlin style sediment-hosted deposits. Economic Geology, 104, 635−668.

Levade, C., Couderc, J.-J., Bras, J., and Fagot, M. (1982) Transmission electron microscopy study of experimentally deformed pyrite. Philosophical Magazine A, 46, 307–25.

Li, W., Cook, N.J., Xie, G.Q., Mao, J.W., Ciobanu, C.L., Li, J.W., and Zhang, Z.Y. (2019) Textures and trace element signatures of pyrite and arsenopyrite from the Gutaishan Au–Sb deposit, South China. Mineralium Deposita, 54, 591-610.

McClay, K.R., and Ellis, P.G. (1983) Deformation and recrystallization of pyrite. Mineralogical Magazine, 47, 527-538.

Meinert, L.D. (2000) Gold in skarns related to epizonal intrusions: Reviews in Economic Geology, 13, 347-375.

Morey, A.A., Tomkins, A.G., Bierlein, F.P., Weinberg, R.F., and Davidson, G.J. (2008) Bimodal distribution of gold in pyrite and arsenopyrite: examples from the Archean Boorara and Bardoc shear systems, Yilgarn Craton, Western Australia. Economic Geology, 103, 599-614.

Morishita, Y., Hammond, N.Q., Momii, K., Konagaya, R., Sano, Y., Takahata, N., and Ueno, H. (2019) Invisible Gold in Pyrite from Epithermal, Banded-Iron-Formation-Hosted, and Sedimentary Gold Deposits: Evidence of Hydrothermal Influence. Minerals, 9, 447.

Palenik, C.S., Utsunomiya, S., Reich, M., Kesler, S.E., and Ewing, R.C. (2004) “Invisible” gold revealed: direct imaging of gold nanoparticles in a Carlin-type deposit. American Mineralogist, 89, 1359–1366.

Pokrovski, G.S., Kokh, M.A., Proux, O., Hazemann, J.-L., Bazarkina, E.F., Testemale, D., Escoda, C., Boiron, M.-C., Blanchard, M., Aigouy, T., Gouy, S., de Parsevala, P., and Thibaut, M. (2019) The nature and partitioning of invisible gold in the pyrite-fluid system. Ore Geology Reviews, 109, 545-563.

Pokrovski, G.S., Escoda, C., Blanchard, M., Testemale, D., Hazemann, J.-L., Gouy, S., Kokh, M.A., Boiron, M.-C., de Parseval, F., Aigouy, T., Menjot, L., de Parseval, P., Proux, O., Rovezzi, M., Béziat, D., Salvi, S., Kouzmanov, K., Bartsch, T., Pöttgen, R., and Doert, T. (2021) An arsenic-driven pump for invisible gold in hydrothermal systems. Geochemical Perspectives Letters, 17, doi: 10.7185/geochemlet.2112.

Pósfai, M., and Buseck, P.R. (1997) Modular structures in sulfides: sphalerite/wurtzite-, pyrite/marcasite-, and pyrrhotite-type minerals. EMU Notes in Mineralogy, 1, 193-235.

Ray, D., Voigt, B., Manno, M., Leighton, C., Aydil, E.S., and Gagliardi, L. (2020) Sulfur Vacancy Clustering and Its Impact on Electronic Properties in Pyrite $FeS_2$. Chemistry of Materials, 32, 4820–4831.

Reddy, S.M., and Hough, R.M. (2013) Microstructural evolution and trace element mobility in Witwatersrand pyrite. Contributions to Mineralogy and Petrology, 166, 1269-1284.

Reich, M., Kesler, S.E., Utsunomiya, S., Palenik, C.S., Chryssoulis, S.L., and Ewing, R.C. (2005) Solubility of gold in arsenian pyrite. Geochimica et Cosmochimica Acta, 69, 2781-2796.

Rogowitz, A., Zaefferer, S., and Dubosq, R. (2018) Direct observation of dislocation nucleation in pyrite using combined electron channelling contrast imaging and electron backscatter diffraction. Terra Nova, 30, 423-430.

Rollog, M., Cook, N.J., Guagliardo, P., Ehrig, K., and Kilburn, M. (2020) Radionuclide distributions in Olympic Dam copper concentrates: the significance of minor hosts, incorporation mechanisms, and the role of mineral surfaces. Minerals Engineering, 148, 106176.

Sung, Y.H, Brugger, J., Ciobanu, C.L., Pring, A., Skinner, W. and Nugus, M. (2009) Invisible gold in arsenian pyrite and arsenopyrite from a multistage Archean gold deposit: Sunrise Dam, Eastern Goldfields Province, Western Australia. Mineralium Deposita, 44, 765-791.

Törmänen, T.O., and Koski, R.A. (2005) Gold enrichment and the Bi–Au association in pyrrhotite-rich massive sulfide deposits, Escanaba Trough, Southern Gorda Ridge. Economic Geology, 100, 1135–1150.

Tomkins, A.G., and Mavrogenes, J.A. (2002) Mobilization of gold as a polymetallic melt during pelite anatexis at the Challenger gold deposit, South Australia: a metamorphosed Archean gold deposit. Economic Geology, 97, 1249–1271.

Tooth, B., Brugger, J., Ciobanu, C.L., and Liu, W. (2008) Modelling of gold-scavenging by bismuth melts coexisting with hydrothermal fluids. Geology, 36, 815–818.

Tooth, B., Ciobanu, C.L., Green, L., O'Neill, B. and Brugger, J. (2011) Bi-melt formation and gold scavenging from hydrothermal fluids: An experimental study. Geochimica et Cosmochimica Acta, 75, 5423-5443.

van Goethem, L., van Landyut, J., and Amelincks, S. (1978) Study of the glide elements in pyrite by means of electron microscopy and electron diffraction. American Mineralogist, 63, 548-550.

Van Tendeloo, G., Gregoriades, P., and Amelinckx, S. (1983) Electron microscopic studies of modulated structures in (Au,Ag)$Te_2$: Part II. Sylvanite $AgAuTe_4$. Journal of Solid State Chemistry, 50, 335-361.

Van Tendeloo, G., Amelinckx, S., and Gregoriades, P. (1984) Electron microscopic studies of modulated structures in (Au,Ag)$Te_2$. III Krennerite Journal of Solid State Chemistry, 53, 281-289.

Verdugo-Ihl, M.R., Ciobanu, C.L., Cook, N.J., Ehrig, K., Courtney-Davies, L., and Gilbert, S. (2017) Textures and U-W-Sn-Mo signatures in hematite from the Cu-U-Au-Ag orebody at Olympic Dam, South Australia: defining the archetype for IOCG deposits. Ore Geology Reviews, 91, 173–195.

Verdugo-Ihl, M.R., Ciobanu, C.L., Cook, N.J., Ehrig, K., and Courtney-Davies, L. (2020) Defining early stages of IOCG systems: evidence from iron-oxides in the outer shell of the Olympic Dam deposit, South Australia. Mineralium Deposita, 55, 429–452.

Voigt, B., Moore, W., Manno, M., Walter, J., Jeremiason, J.D., Aydil, E.S., and Leighton, C. (2019) Transport Evidence for Sulfur Vacancies as the Origin of Unintentional n-Type Doping in Pyrite $FeS_2$. ACS Applied Materials Interfaces, 11, 15552–15563.

Wu, Y.-F., Evans, K., Hu, S.-Y., Fougerouse, D., Zhou, M.-F., Fisher, L.A., Guagliardo, P., and Li, J.-W. (2021) Decoupling of Au and As during rapid pyrite crystallization. Geology, 49, 827-831.

Xing, Y., Brugger, J., Tomkins, A., and Shvarov, T. (2019) Arsenic evolution as a tool for understanding formation of pyritic gold ores. Geology, 47, 335–338.

712 **Figure captions**

713 **Figure 1.** Reflected light photomicrographs showing the analyzed sample (a) and details of pyrite textures (b-
714 k). Numbered circles in (a) represent pyrites analyzed by LA-ICP-MS (Online Material[1] Table 1). (b-e)
715 Variable textures resulting from marginal replacement of brecciated pyrite (Py) by chalcopyrite (Cp), from
716 incipient (b) to advanced (e). (f, g) Sulfide disseminations surrounding hematite (Hm) clasts, displaying brittle
717 fracturing, marginal milling and grain rounding. Note the presence of μm-sized magnetite (Mt) within such
718 clasts. Replacement of pyrite by chalcopyrite during milling is supported by textures showing ductile behavior
719 of chalcopyrite at junctions of Hm clasts in (h). (i-k) Details of micron-scale textures in pyrite showing domains
720 preserving oscillatory zoning (below the dashed line in i), sub-micron sized chalcopyrite inclusions (arrowed
721 in j) and patchy zoning within porous areas (dashed lines in k.

722 **Figure 2.** (a) Reflected light photomicrograph showing pyrite Py67a with incipient chalcopyrite (Cp)
723 replacement. FIB cuts marked as numbered black lines. Note sub-grains (dotted line) within this pyrite (Py)
724 which otherwise displays a sub-euhedral outline. (b) BSE image showing the contact between zoned, sub-
725 grains. Note coarse inclusions (black) and darkening of pyrite along the boundary. Short arrows indicate the
726 boundary interval along the FIB cut. (c, d) BSE images of Py37 with patchy oscillatory zoning (detail in c).
727 White and yellow arrows in (c) show sub-μm inclusions and pores, respectively. (e) LA-ICP-MS element
728 maps for As and Au for Py37 mirroring the textures in (d) and showing overlap between the two elements.
729 Scales in counts per second (cps, $10^n$); see methodology in Online Material[1] Figure A1. (f) Plot of Au vs. As.
730 Yellow spots indicate high-Au domains within pyrite grains analysed at nanoscale. (g) Representative time-
731 resolved downhole LA-ICP-MS profile. Note smooth Au signal.

732 **Figure 3. (a)** Hierarchical cluster dendrogram showing the association of the 14 targeted trace elements for
733 the LA-ICP-MS dataset (Online Material[1] Table A1). The similarity among the elements is reflected by the
734 height of the dendrogram that corresponds to the variation matrix (Online Material[1] Table A2). (b) Box plots
735 of concentrations of groups of trace elements in pyrite based on l the three optimal clusters. Clusters 1 and 3
736 are geochemically similar but Cluster 3 is distinct in terms of the highest median concentration of Sn (median,
737 8.6 ppm) and Bi (not shown on boxplot, median, 18 ppm). (c, d) PC1 versus PC2 diagrams showing principal
738 component scores in (c) and loadings in (d) of the clr-transformed LA-ICP-MS data. Scores are colored
739 according to clusters derived via k-means algorithms.

740 **Figure 4.** (a, b) BSE images showing further textural details of the two Au-As-bearing pyrites sampled for the
741 nanoscale study. Note mosaic-dissolution boundaries (yellow dashed lines) typical of Py37 and inner parts of
742 sub-grains (outlined in blue) in Py67a. Orientation of the three sub-grains at 120º to one another also marked
743 by the triple arrows. (c-f) HAADF STEM images of the four foils obtained from locations as marked in (a, b).
744 Grain boundaries (white dashed lines) and other textures are also marked and labelled. Abbreviations:
745 Cob=cobaltite; Cp=chalcopyrite; Py=pyrite; sulfotell.=sulfotelluride; tell.=telluride.

746 **Figure 5.** Images and STEM EDS element maps of pyrite domains showing different types of compositional
747 zonation patterns. Locations of maps marked in Figure 4. (a) Primary oscillatory zoning with respect to As and

Co (Ni not shown) in foil #1 (Py37; map 0003). Inclusions outlined in red and arrowed. (b) New growth of an unzoned, As-bearing grain along the dissolution boundary in Py67a (map 1406; foil #2). (c) Element maps for As and Co showing fine oscillatory zoning with Co-bearing inclusion (Py67a; map 1716; foil #3). (d) New growth highlighted by As and Co zoning in Py67a (map 1756; foil #4). Note Co-NPs along the boundaries and splays with Co-enrichment.

**Figure 6.** HAADF STEM images, except the first panel in (a) which is a BF image, showing nanotextures and inclusions in the two As-Au bearing pyrites. Brighter contrast on HAADF images correlates with the presence of elements with higher Z than those present in stoichiometric pyrite (Fe, S). (a) Sets of duplex splays (arrowed) crosscutting grain boundaries. (b) Sets of splays crosscutting primary zoning in pyrite (shown in Figure 5a). Inclusions are marked. (c) High-resolution image showing sets of rhythmically misorientation planes (arrowed). (d-i) Inclusions and particles of variable composition and sizes as labelled associated with splays (dashed lines) or pores (in d and e). Note the trail of Bi-NPs leading to NPs coating the large pore in (e). (j, k) Nanostructures (dashed line) enriched in precious metals and associated Te, Bi and Pb. Abbreviations: Cst=cassiterite; Cp=chalcopyrite; El=electrum; sulfotell.=sulfotelluride

**Figure 7.** BF STEM images, except lower part of (a) and insets in (f-h and l) which are HAADF images, showing the range of nanotextures and their orientations associated with trace element (re)mobilization and particle nucleation. Orientation of pyrite is given as zone axis in square brackets. (a-b) Dissolution boundary with dipoles at the junction between grains at a dissolution-reprecipitation boundary. The area in (a) corresponds to the map in Figure 5d. (c) *En-echelon* microcracks along dissolution boundary shown on map in Figure 5c. (d-e) Dipoles of variable orientation, splitting into duplexes and/or loops. Hosted inclusions outlined in yellow. Coarse Bi-Pb-sulfotelluride (inset in f) at edge of radial dipole. (g-i) More complex arrays of dislocations leading to inclusion nucleation as labelled. Note twist-wall boundary in (h) leading to enrichment in Bi-Pb-Te (inset). (j-m) Au-Ag-NPs (yellow outline, inset in (l) associated with dislocation nucleation on slip planes. Note variation in arrangement of dislocations within a zone from parallel sets (j and l), through conjugate (k) to low-angle slip planes (m). The latter hosts the most abundant Au-bearing NPs. Abbreviations: Cob=cobaltite; Fe-oxide=iron oxide.

**Figure 8.** STEM EDS maps showing aspects of trace element (re)mobilization accompanying formation of Au-bearing NPs along nanostructures. (a) Bi, Te, Ag-bearing galena NP along splays crosscutting primary zoning in pyrite (area shown in Figure 5a). Note trails of the same elements, in particular Bi and Pb (dashed line) dissipating away and/or towards the NP. (b) HAADF STEM image and element maps showing a 2-3 nm-wide dislocation plane in pyrite that is relatively enriched in Bi, Te, Pb (inner part) and also Co (broader, outer area). (c) HAADF STEM image and element maps showing Au-Ag-telluride NP (petzite) along splays with As and Co (re)mobilization. Note Co is prominent in highlighting the splays, whereas As is concentrated at the edges of the NP.

**Figure 9.** HAADF-STEM images and STEM EDS element maps showing various inclusions in As-Au-rich pyrites. (a) Smallest NPs as electrum (El) within nanopores from a chalcopyrite (Cp) inclusion. (b) Large pore coated with Bi-Ag-telluride NPs (volynskite; Vol?). Electrum NPs around the margins of the hole are circled.

(c) Image and maps of the largest (~5 nm-wide) electrum NP from (b). (d) NPs association comprising two Au-Ag-tellurides, petzite (Ptz) and sylvanite (Syl), and a Bi-Pb-sulfotelluride (Bi-Pb-tell). (e) Bi-Pb-sulfotelluride showing the layered structure in terms of main elements. Note Bi correlates with Te, and Pb correlates with S. (f) Cassiterite NP with a marginal Te rim (arrowed) and coating of NaCl. Note that such coating corresponds to the darker part of the NP on the HAADF STEM image to the right.

**Figure 10**. Atomic-scale imaging of defects associated with trace element (re)mobilization in As-Au-rich pyrite (Py67a in a-d, Py37 in e-g). Insets in a and e show Fast Fourier transform (FFT) patterns of pyrite in the corresponding image. (a, b) Slip plane (~1 nm-wide) in pyrite enriched in trace elements as labelled (corresponding to map in Figure 5b). Note high diffraction contrast indicative of atom dislocation perpendicular to the plane trace on the BF image (a) and the brightness of this plane on the HAADF image (b). (c, d) HAADF STEM images showing nucleation of wider (several nm-wide) lamellae of Bi-Pb-sulfotellurides along kinked dipoles (shown in Figure 7d). Note smearing of heavy elements (Bi, Pb, and Te) at the junction between planes (in c). In (d) ordering of atoms within the sulfotelluride across with a split of Fe atoms in the pyrite is marked by dashed lines across the dipole. (e-g) HAADF STEM images showing screw dislocation planes along <100> directions in pyrite from the area shown in Figures 5a and 6b. (f) is a close-up of the arrowed screw dislocation in (e) showing enrichment in heavy elements (brighter contrast). (g) Brighter contrast at the edge of an area with screw dislocations. Step-overs marked by yellow lines.

**Figure 11.** Atomic-scale HAADF STEM images of Au-Ag-tellurides (a, b) and a Bi-Pb-sulfotelluride (c, d). FFT patterns as insets in (a-c). Note coherent intergrowths between pyrite and Au-Ag-tellurides in (a). Numbers in (c) correspond to atom layers within the sulfotelluride (see main text). Schematic in (d) shows the atom sequence along 7- and 9-atom layers from the area outlined in black. Ptz=petzite; Py=pyrite; Syl=sylvanite.

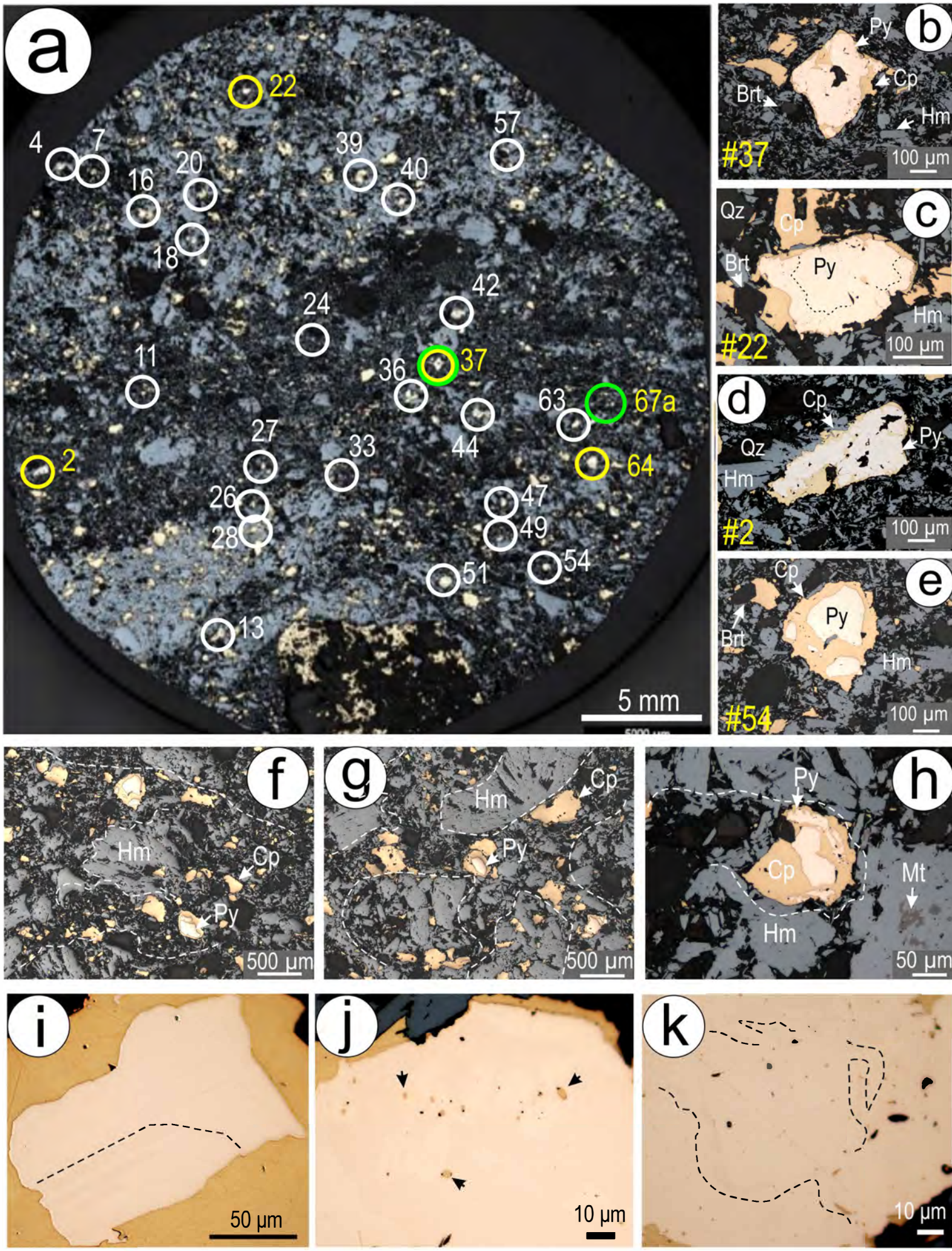


Figure 1 Ehrig et al.

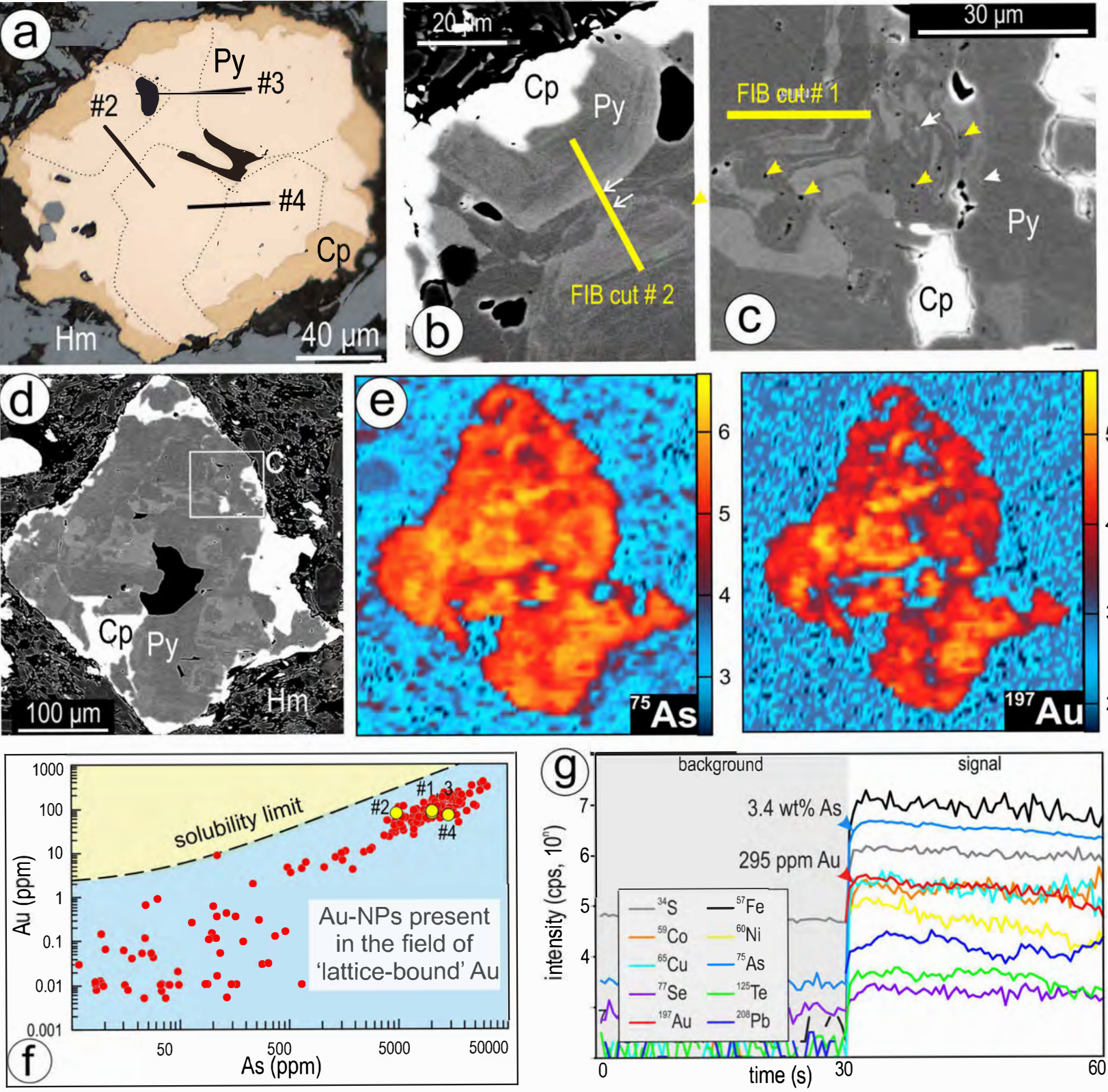


Figure 2 Ehrig et al.

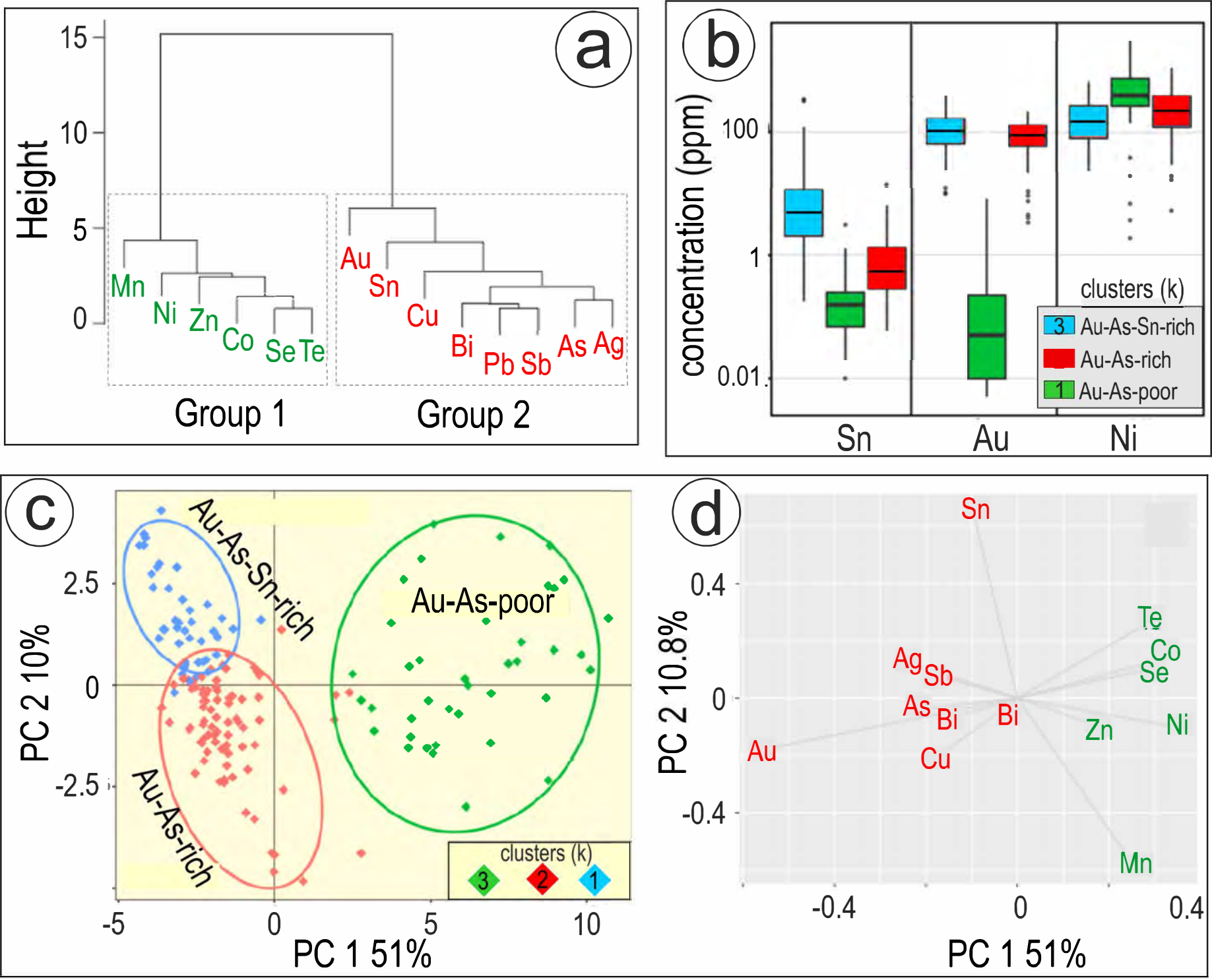


Figure 3 Ehrig et al.

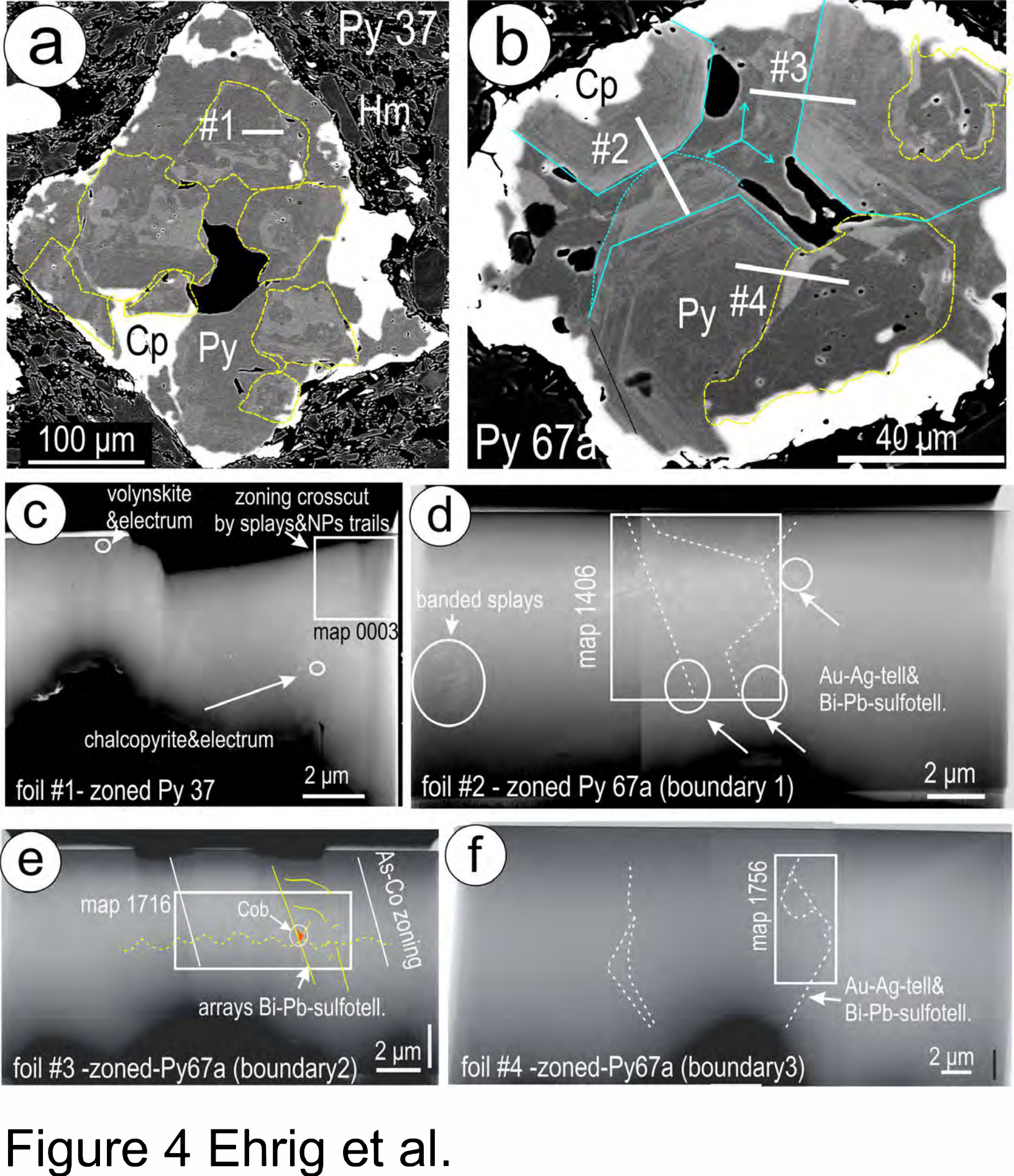


Figure 4 Ehrig et al.

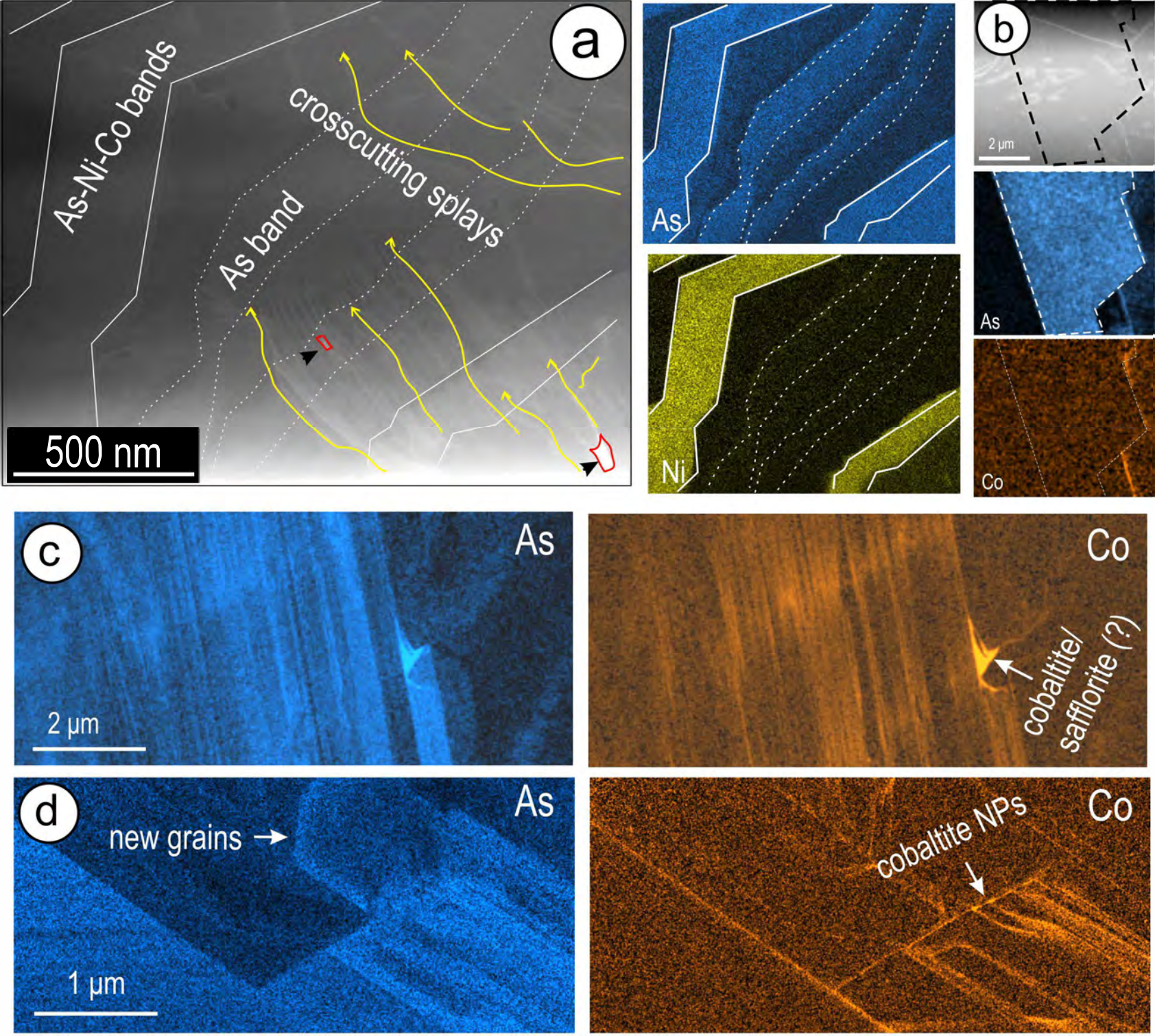


Figure 5 Ehrig et al.

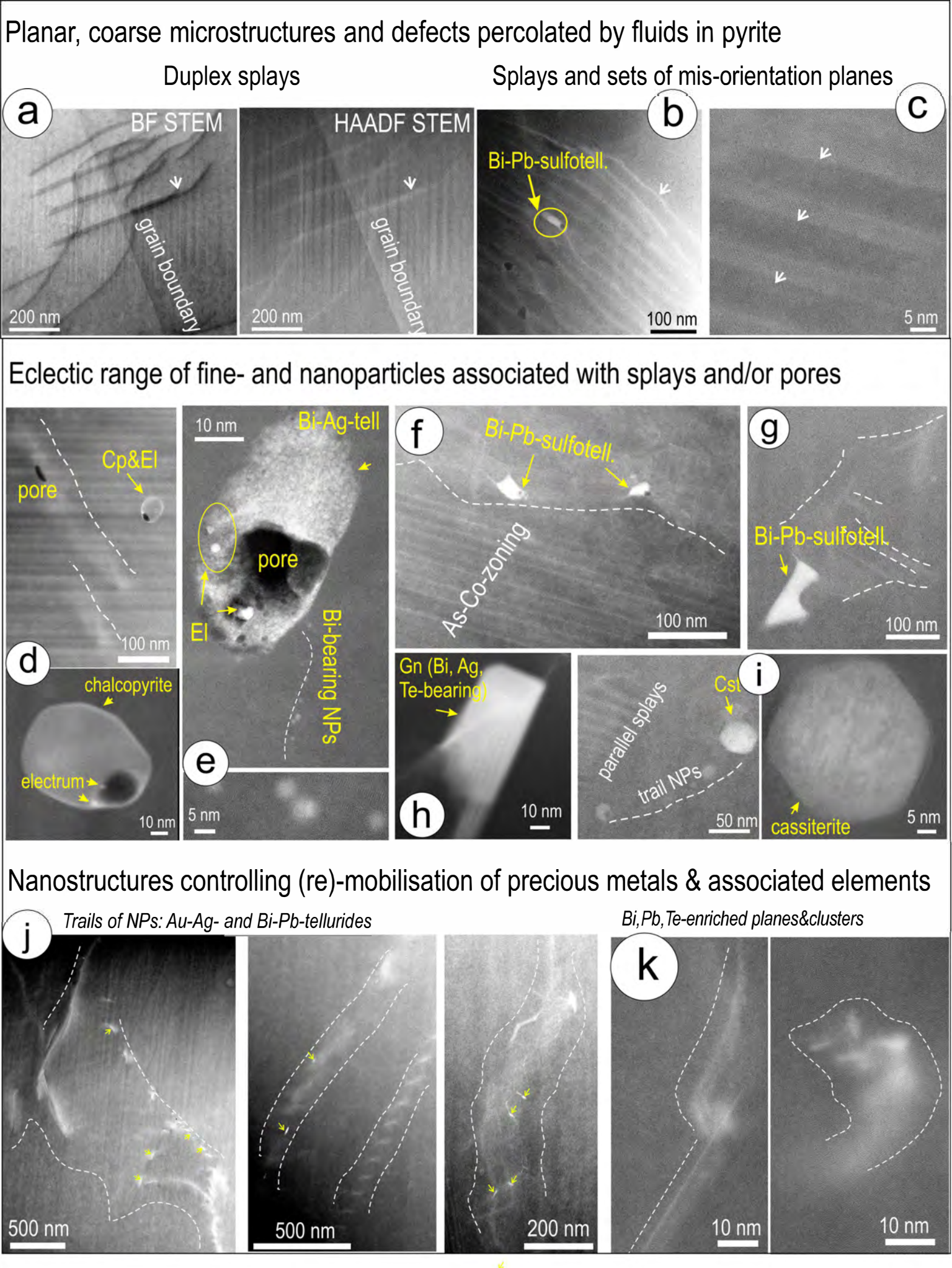


Figure 6 Ehrig et al.

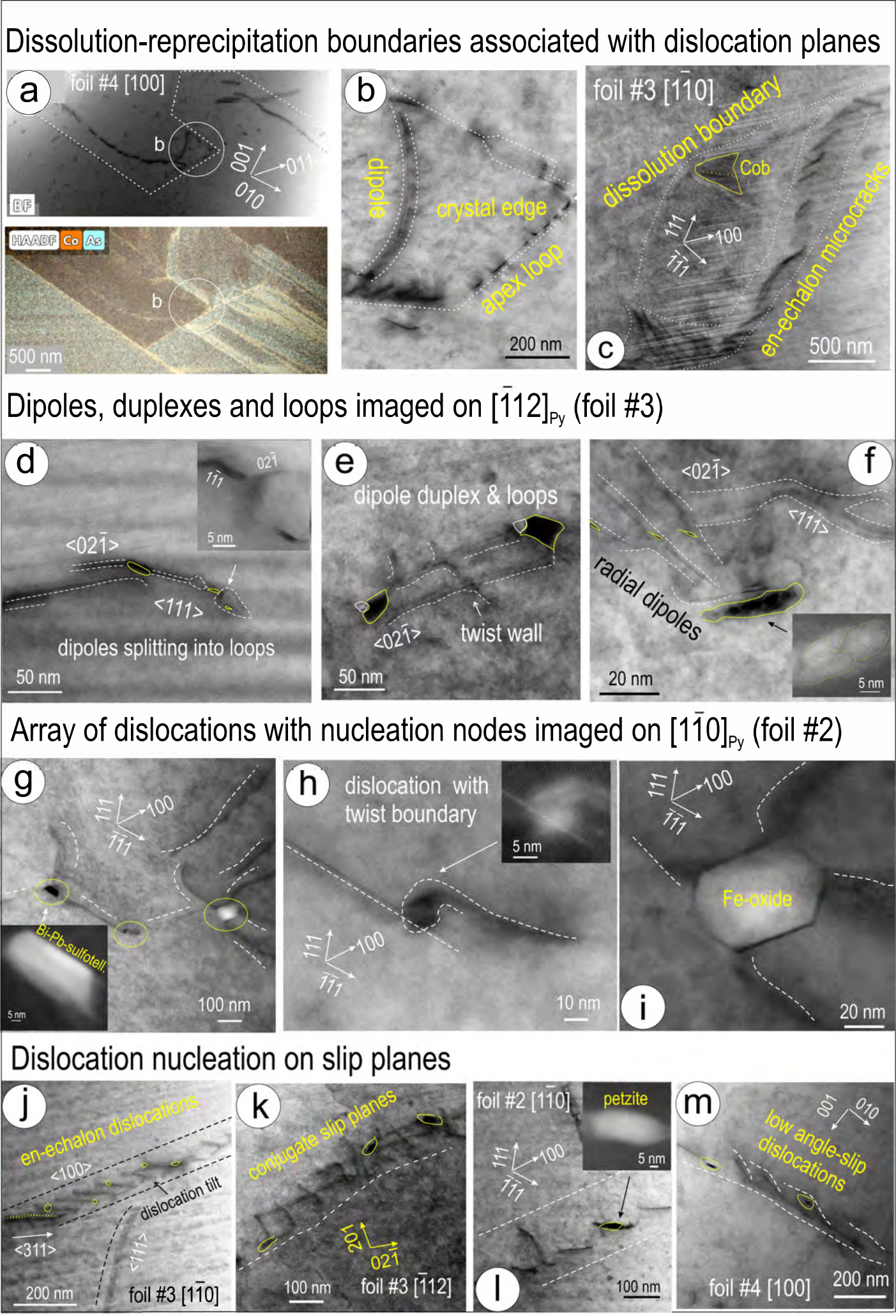


Figure 7 Ehrig et al.

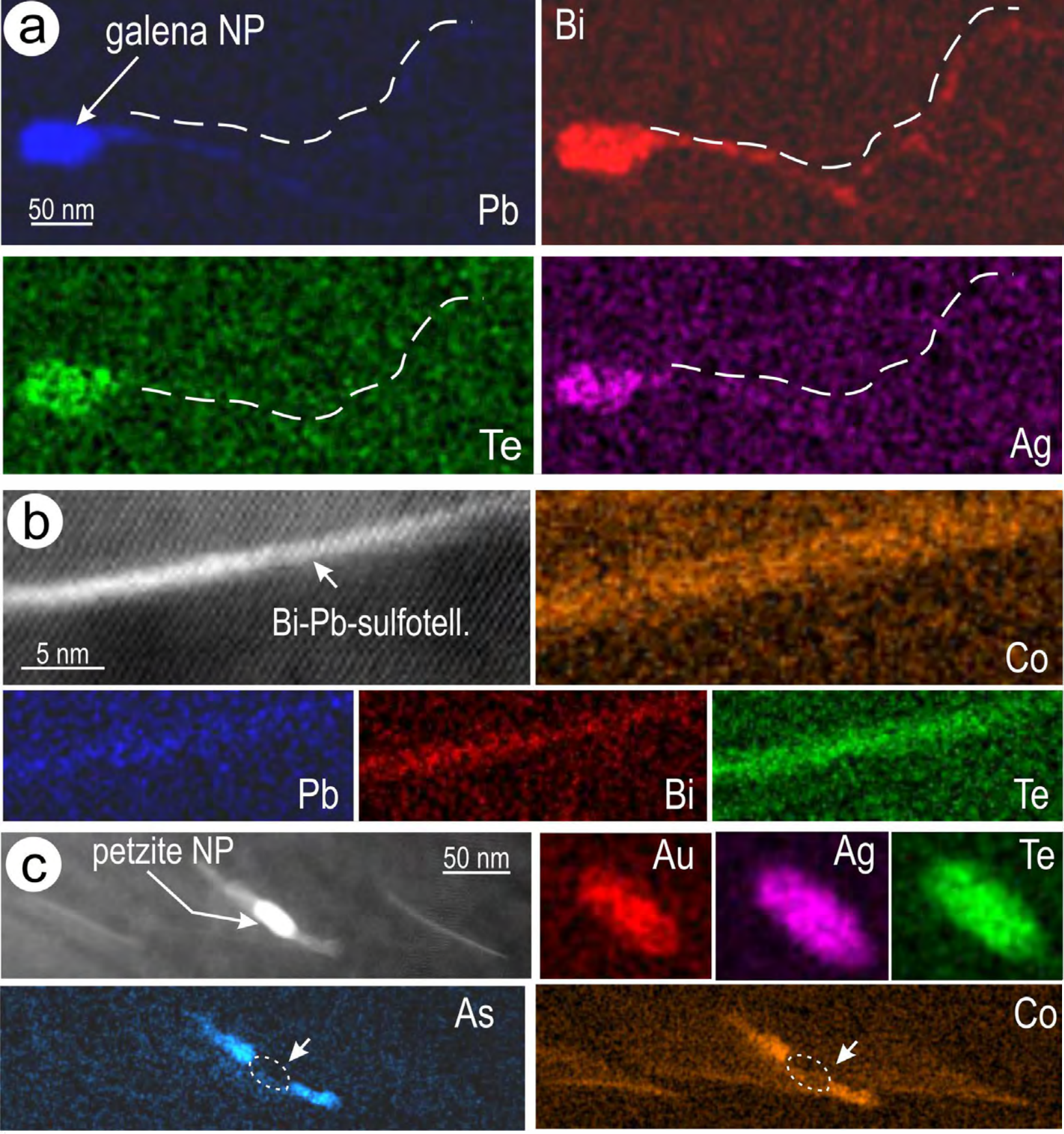


Figure 8 Ehrig et al.

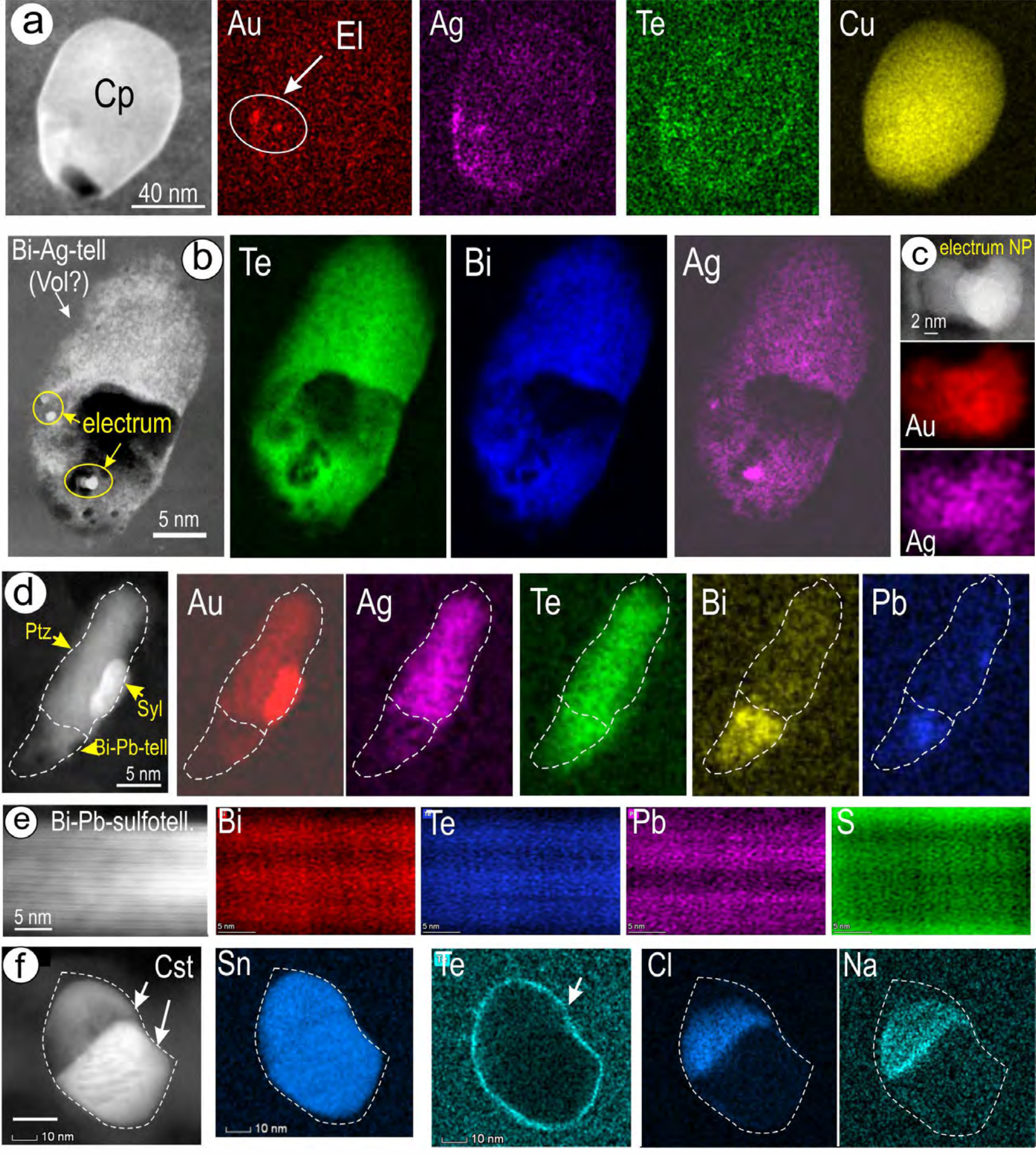


Figure 9 Ehrig et al.

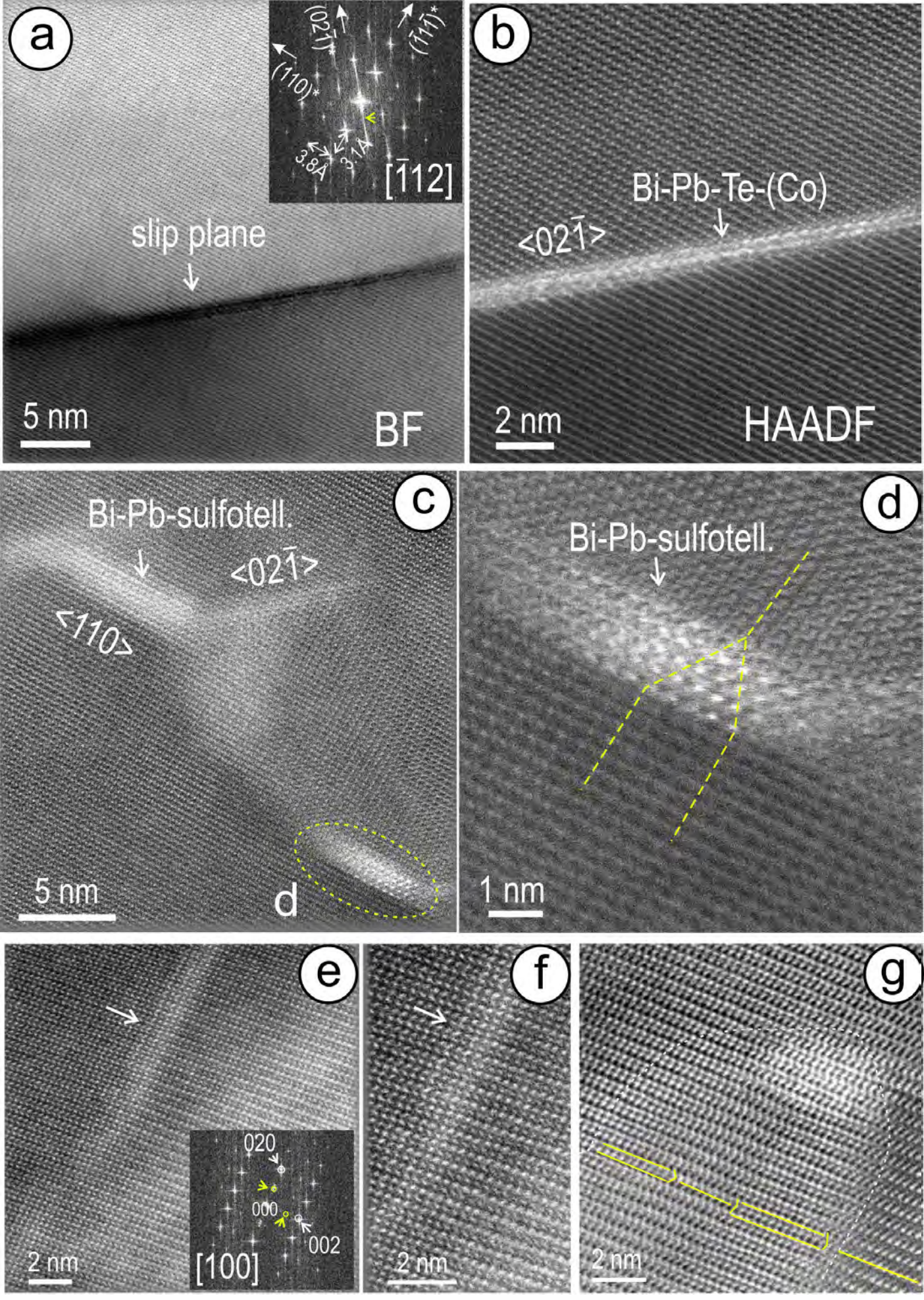


Figure 10 Ehrig et al.

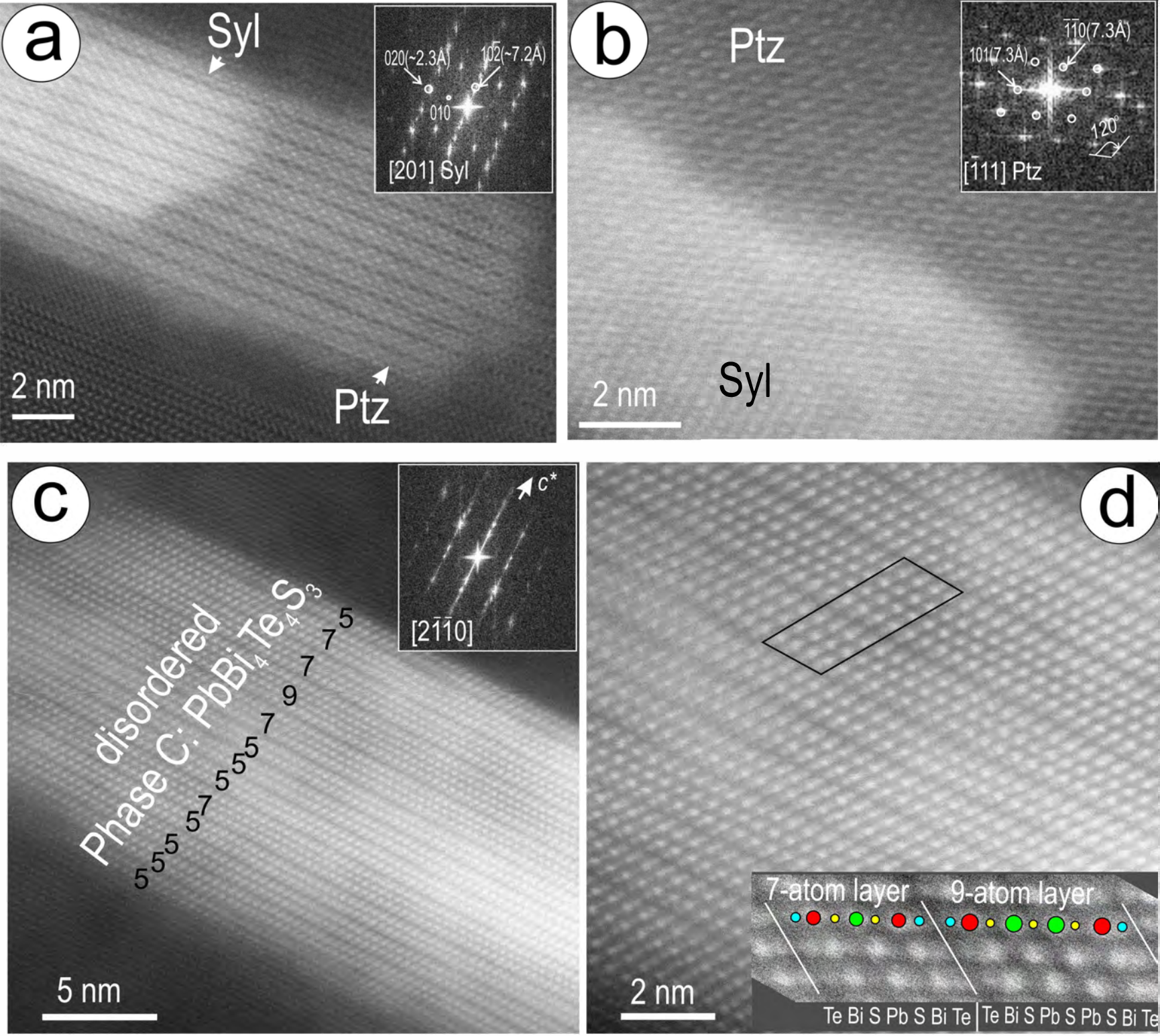


Figure 11 Ehrig et al.